Persistent Nav1.1 and Nav1.6 currents drive spinal locomotor functions through nonlinear dynamics

Benoît Drouillas, Cécile Brocard, Sébastien Zanella, Rémi Bos, Frédéric Brocard

To cite this version:

Benoît Drouillas, Cécile Brocard, Sébastien Zanella, Rémi Bos, Frédéric Brocard. Persistent Nav1.1 and Nav1.6 currents drive spinal locomotor functions through nonlinear dynamics. Cell Reports, 2023, 42 (9), pp.113085. 10.1016/j.celrep.2023.113085 . hal-04245363

HAL Id: hal-04245363
https://hal.science/hal-04245363v1

Submitted on 17 Oct 2023

Cell Reports

Article

Persistent Nav1.1 and Nav1.6 currents drive spinal locomotor functions through nonlinear dynamics

Graphical abstract

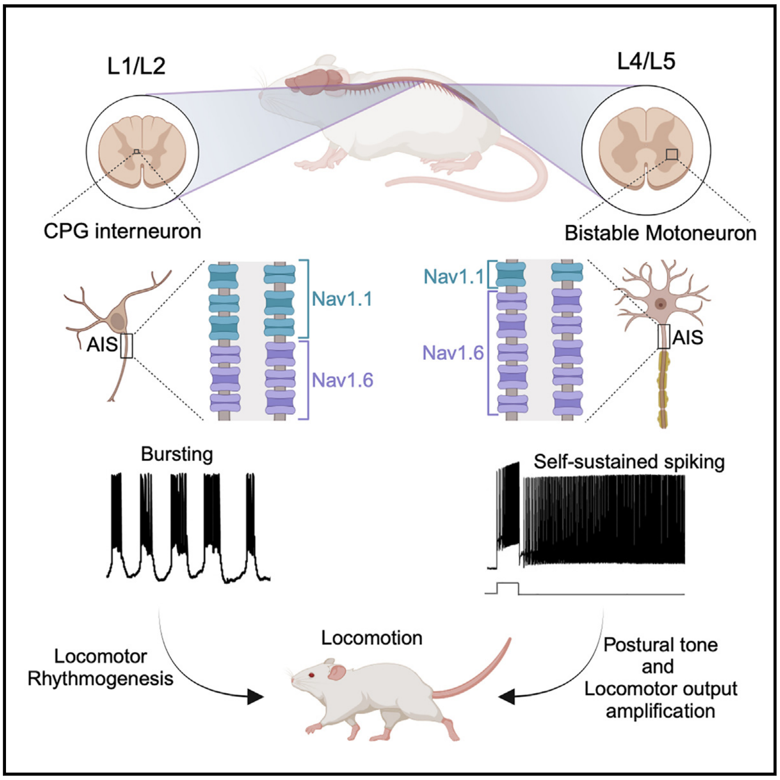

Highlights

- *Nav1.6* mediates I_{NaP} and self-sustained spiking activity in bistable motoneurons
- Silencing *Nav1.6* in spinal motoneurons alters posture and locomotor performance
- *Nav1.6* works with *Nav1.1* to mediate I_{NaP} and bursting pacemakers within locomotor CPG
- The *Nav1.1-Nav1.6* partnership generates the locomotor rhythm

Authors

Benoît Drouillas, Cécile Brocard, Sébastien Zanella, Rémi Bos, Frédéric Brocard

Correspondence

frederic.brocard@univ-amu.fr

In brief

Drouillas et al. show how *Nav1.1* and *Nav1.6* channels regulate spinal locomotor activity. *Nav1.6*, by mediating persistent sodium current (I_{NaP}) in bistable motoneurons, produces postural tone and amplifies locomotor outputs. Together with *Nav1.1*, it drives the locomotor rhythm by mediating I_{NaP}-dependent bursting activities in interneurons of the central pattern generator.

Drouillas et al., 2023, Cell Reports *42*, 113085
September 26, 2023 © 2023 The Author(s).
https://doi.org/10.1016/j.celrep.2023.113085

CellPress

Cell Reports

CellPress
OPEN ACCESS

Article

Persistent Nav1.1 and Nav1.6 currents drive spinal locomotor functions through nonlinear dynamics

Benoît Drouillas,[1] **Cécile Brocard,**[1] **Sébastien Zanella,**[1] **Rémi Bos,**[1] **and Frédéric Brocard**[1,2,*]

[1] Institut de Neurosciences de la Timone, UMR 7289, Aix-Marseille Université and Centre National de la Recherche Scientifique (CNRS), Marseille, France

[2] Lead contact

*Correspondence: frederic.brocard@univ-amu.fr

https://doi.org/10.1016/j.celrep.2023.113085

SUMMARY

Persistent sodium current (I_{NaP}) in the spinal locomotor network promotes two distinct nonlinear firing patterns: a self-sustained spiking triggered by a brief excitation in bistable motoneurons and bursting oscillations in interneurons of the central pattern generator (CPG). Here, we identify the NaV channels responsible for I_{NaP} and their role in motor behaviors. We report the axonal *Nav1.6* as the main molecular player for I_{NaP} in lumbar motoneurons. The inhibition of *Nav1.6*, but not of *Nav1.1*, in motoneurons impairs I_{NaP}, bistability, postural tone, and locomotor performance. In interneurons of the rhythmogenic CPG region, both *Nav1.6* and *Nav1.1* equally mediate I_{NaP}. Inhibition of both channels is required to abolish oscillatory bursting activities and the locomotor rhythm. Overall, *Nav1.6* plays a significant role both in posture and locomotion by governing I_{NaP}-dependent bistability in motoneurons and working in tandem with *Nav1.1* to provide I_{NaP}-dependent rhythmogenic properties of the CPG.

INTRODUCTION

The spinal central pattern generator (CPG) is a neural network that plays a pivotal role in generating rhythmic motor patterns, essential for locomotion in vertebrates. The CPG operates autonomously but can be modulated by sensory feedback and higher brain centers, ensuring adaptability to environmental needs.[1,2] Positioned downstream of the CPG, motoneurons act as the "final pathway", relaying CPG commands to the muscles to initiate movement.

Within motor CPGs, rhythm generation is theorized to emerge from two primary mechanisms.[3,4] The "emergent properties" mechanism proposes that rhythmic activity is a consequence of the synergistic interactions between excitatory and inhibitory interneurons, with no individual neuron inherently possessing rhythmic characteristics. On the other side, the "pacemaker-driven" hypothesis contends that specific neurons or neuron clusters, characterized by distinct ion channel dynamics, intrinsically manifest rhythmic behaviors, subsequently shaping the rhythmic activity across the entire network. These two mechanisms, while distinct, might not operate in isolation. Recent studies suggest an interplay between the global network dynamics and the innate attributes of individual neurons, playing a pivotal role in determining the rhythmic locomotor outputs of the CPG.[5,6]

Central to the rhythmogenic module of the locomotor CPG are a group of excitatory interneurons exhibiting membrane oscillations within a frequency range congruent with typical locomotor rhythms, primarily due to the persistent sodium current (I_{NaP}).[4–11] The pivotal role of I_{NaP} in locomotion becomes even more evident when observing that an activity-dependent increase of I_{NaP} coincides with the emergence of the locomotor rhythm.[5,8] Conversely, inhibiting I_{NaP} in vertebrates leads to a marked disruption in this rhythm, emphasizing its critical nature in the locomotion process.[6,12–16] These findings collectively highlight the fundamental role of I_{NaP} in driving the locomotor rhythm, primarily by fostering neuronal oscillations within the CPG. However, the role of I_{NaP} is not limited to rhythm generation alone. It also plays a crucial role in amplifying synaptic current, notably by facilitating a self-sustained spiking activity in spinal motoneurons, which can be initiated by a brief excitatory input.[17–19] This bistable behavior has recently been shown to be linked to the maintenance of postural tone in the hindlimbs.[20] In sum, in agreement with motor dysfunctions often associated with its alteration,[21–27] I_{NaP} appears to be critical for the operation of the spinal locomotor network in vertebrates.

Despite our progress in understanding the functional roles played by I_{NaP} within the spinal locomotor network, there remains a significant gap in our understanding of the specific Nav channel isoforms that contribute to I_{NaP}. Among the nine α-subunits, *Nav1.1*, *Nav1.2*, *Nav1.3*, and *Nav1.6* predominate in the CNS.[28] We focused on *Nav1.1* and *Nav1.6* because of their strong expression within the ventral spinal cord,[29–33] while *Nav1.2* and *Nav1.3* are predominantly found in dorsal horn sensory neurons.[30,31,33] Here, we identified Nav1.6 as the molecular constituent of I_{NaP} in bistable motoneurons and provided

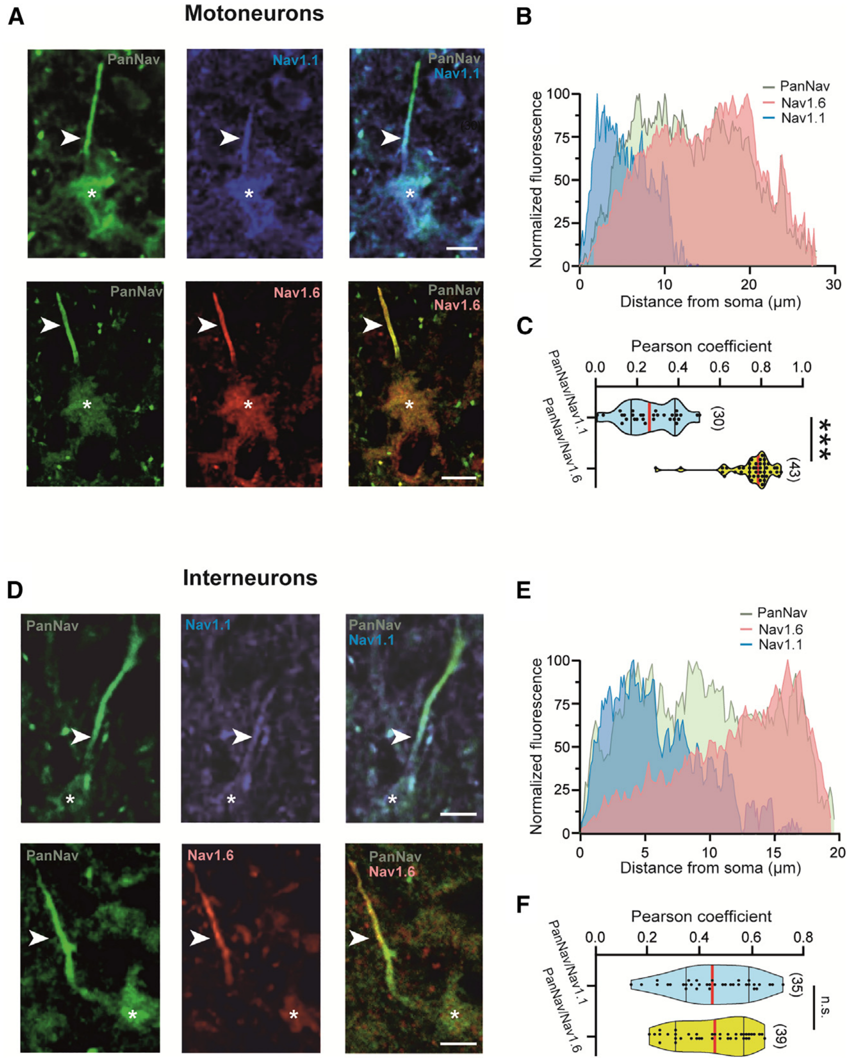

Figure 1. Distribution of *Nav1.1* and *Nav1.6* subunits in the axon initial segments (AISs) of lumbar motoneurons and interneurons of the rhythmogenic CPG region for locomotion

(A and D) Representative optical sections showing the immunostaining of all Nav α-subunits (left, green), *Nav1.1* subunits (top middle, blue), or *Nav1.6* subunits (bottom middle, red) along the AISs (arrowheads) of lumbar L4/L5 motoneurons (A) or L1/L2 ventromedial interneurons (D). The right panels are merged images. Scale bars represent 10 µm for (A) and 5 µm for (D).

(B and E) The mean fluorescence intensity profile for the PanNav (green), *Nav1.1* (blue), and *Nav1.6* (red) immunostainings along the PanNav-labeled AIS of motoneurons (B, n = 12 cells) and interneurons (E, n = 12 cells). For each antibody, the immunofluorescence was normalized to its maximum intensity.

(C and F) Violin plots of the Pearson's coefficient between PanNav and Na1.1 (cyan) or between PanNav and *Nav1.6* (yellow) in motoneurons (C, n = 30–43 cells) and interneurons (F, n = 35–39 cells).

Numbers in brackets in (C) and (F) indicate the numbers of neurons. Each dot in (C) and (F) represents an individual neuron. n.s., no significance; ***p < 0.001 (unpaired t test for C and F).

See also Figures S1 and S2.

evidence of its critical role in promoting self-sustained spiking to support a postural tone in hindlimbs. We also found *Nav1.6* working in tandem with *Nav1.1* within the CPG to produce both I_{NaP}-dependent oscillations at the neuronal level and the locomotor rhythm at the network level.

RESULTS

Nav1.6 expression predominates in lumbar motoneurons

To study the subcellular distribution of the two main sodium channels (*Nav1.1* and *Nav1.6*) of the ventral spinal cord,[30,31] we performed immunohistochemistry both in lumbar motoneurons (L_4–L_5) and interneurons of the rhythmogenic CPG region (L_1–L_2) for locomotion. The pan-specific antibody (PanNav) highlighted all Nav channel isoforms along ankyrin-G-positive axon initial segments (AISs; Figures S1A–S1D). The distribution of *Nav1.1* and *Nav1.6* channels is segregated in motoneurons (Figure 1A). *Nav1.1* was expressed proximally within the first 10 µM of the PanNav staining, while *Nav1.6* mostly paralleled the staining profile of the PanNav along the AIS (Figures 1A and 1B). Specifically, *Nav1.6* gradually increased in density in the first 20 µm and declined in the last 10 µm (Figure 1B). As a result, the PanNav colocalized more extensively with *Nav1.6* than with *Nav1.1* (Figure 1C). In interneurons of the rhythmogenic CPG region located in the ventromedial part of the upper lumbar segments,[34,35] *Nav1.1* and *Nav1.6* were expressed mainly within the first and the second half of the PanNav staining, respectively (Figures 1D and 1E). The distribution of the PanNav staining uniform along the AIS results from this complementary gradient (Figure 1E). Thus, PanNav exhibited an equal colocalization with *Nav1.1* and *Nav1.6* (Figure 1F).

Altogether, the *Nav1.6* channels predominate in lumbar motoneurons, while the relative expression of *Nav1.1* and *Nav1.6* appears more balanced in interneurons of the rhythmogenic CPG region. This observation holds true across the entire lumbar enlargement (Figure S1E).

Nav1.6 channels are instrumental for bistability in motoneurons

To explore the biological significance of *Nav1.1* and *Nav1.6* in firing properties of spinal neurons, we used ICA-121431 (ICA) and 4,9-anhydrotetrodotoxin (4,9-ahTTX) as blockers of *Nav1.1* and *Nav1.6*, respectively.[36–38] We defined the specific and optimal concentration of ICA and 4,9-ahTTX as the highest dose that did not affect characteristics of the spike in $Nav1.1^{-/-}$ and $Nav1.6^{-/-}$ motoneurons, respectively. Before proceeding

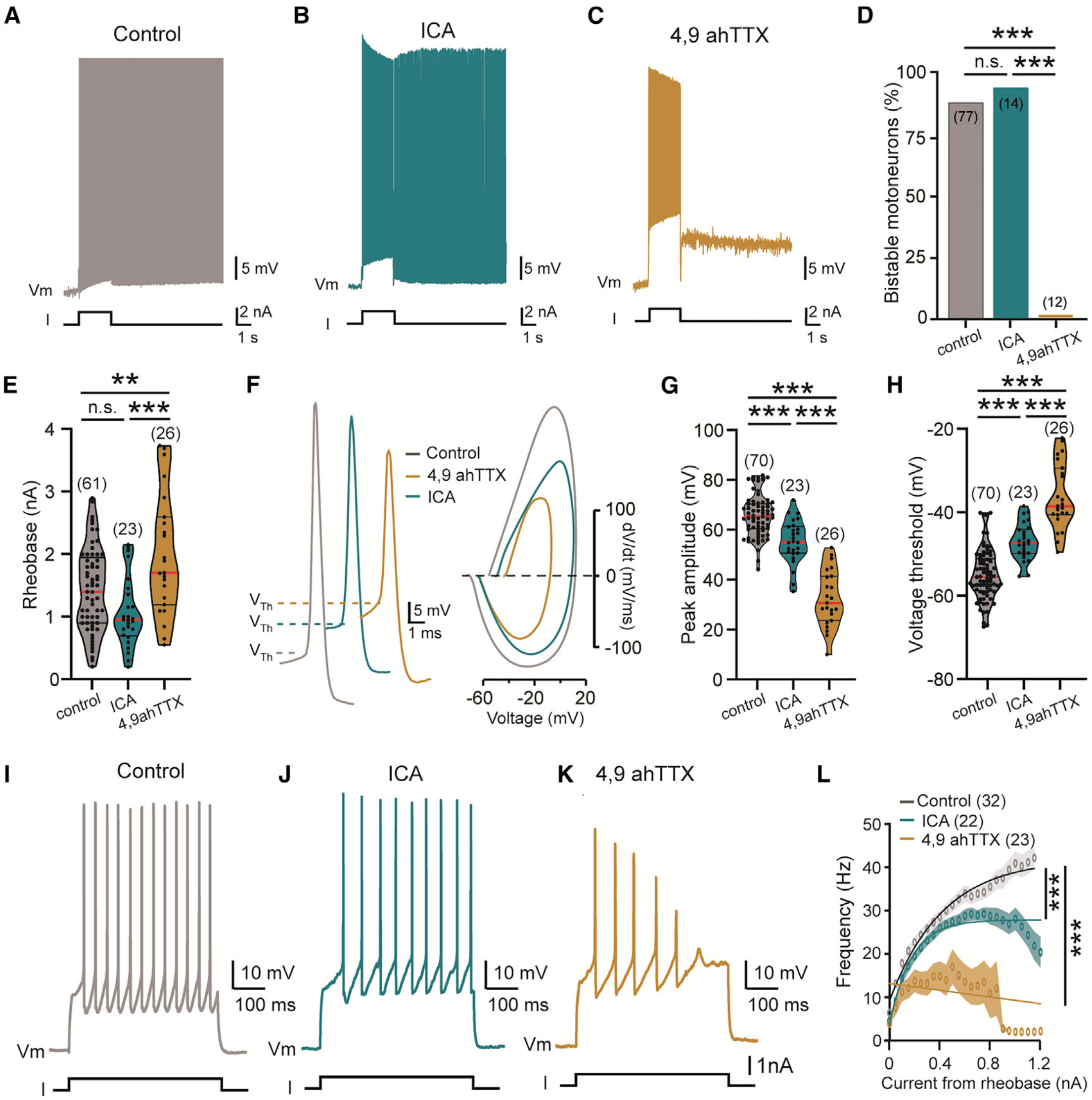

Figure 2. ***Nav1.6* channels are instrumental for bistability in lumbar motoneurons**

(A–C, F, and I–K) Voltage traces from motoneurons recorded in response to suprathreshold (A–C), near-threshold (F), or incrementing (I–K) depolarizing pulses before (A, F, and I, gray, n = 6 mice) or during bath application of ICA-121431 (ICA) (B, F, and J, green, 350 nM, n = 4 mice) or 4,9-anhydrotetrodotoxin (4,9-ahTTX) (C, F, and K, orange, 200 nM, n = 4 mice).

(D) Quantification of the proportion of bistable motoneurons (n = 12–77 cells).

(E, G, and H) Violin plots of the rheobase (E), peak amplitude (G), and threshold (H) of the action potential (n = 23–70 cells).

(F) Representative individual action potentials (left) with their phase plots (right) generated from the first derivative (dV/dt; y axis) versus membrane potential (mV; x axis). Dashed lines indicate the spiking threshold (V_{Th}).

(L) Firing frequency as a function of the amplitude of the current pulse (n = 22–32 cells).

Numbers in brackets in (D), (E), (G), (H), and (L) indicate the number of motoneurons. Each dot in (E), (G), and (H) represents an individual motoneuron. Continuous lines in (L) represent best-fit functions for experimental data with 95% confidence interval. n.s., no significance; $^{**}p < 0.01$; $^{***}p < 0.001$ (two-tailed Fisher test for D; one-way ANOVA with multiple comparisons for E, G, and H; comparison of the fits for L).

See also Figure S4.

with the pharmacological experiments, we ensured by immunohistochemistry the complete absence of the *Nav1.1* and *Nav1.6* channels in the *Nav1.1* and *Nav1.6* knockout mice, respectively (Figures S2A and S2B). From a dose-response curve, the optimal concentration was established at 350 nM for ICA and at 200 nM for 4,9-ahTTX (Figure S3). As we previously reported,[17,20] most of the large motoneurons (~90%) displayed a self-sustained spiking activity dependent on I_{NaP} and triggered by a brief excitation (Figure 2A). This bistability was insensitive to ICA but abolished by 4,9-ahTTX (Figures 2B–2D). The *Nav1.6* blocker decreased the excitability of motoneurons (Figure 2E) and altered both waveform and dynamics of the spike more strongly

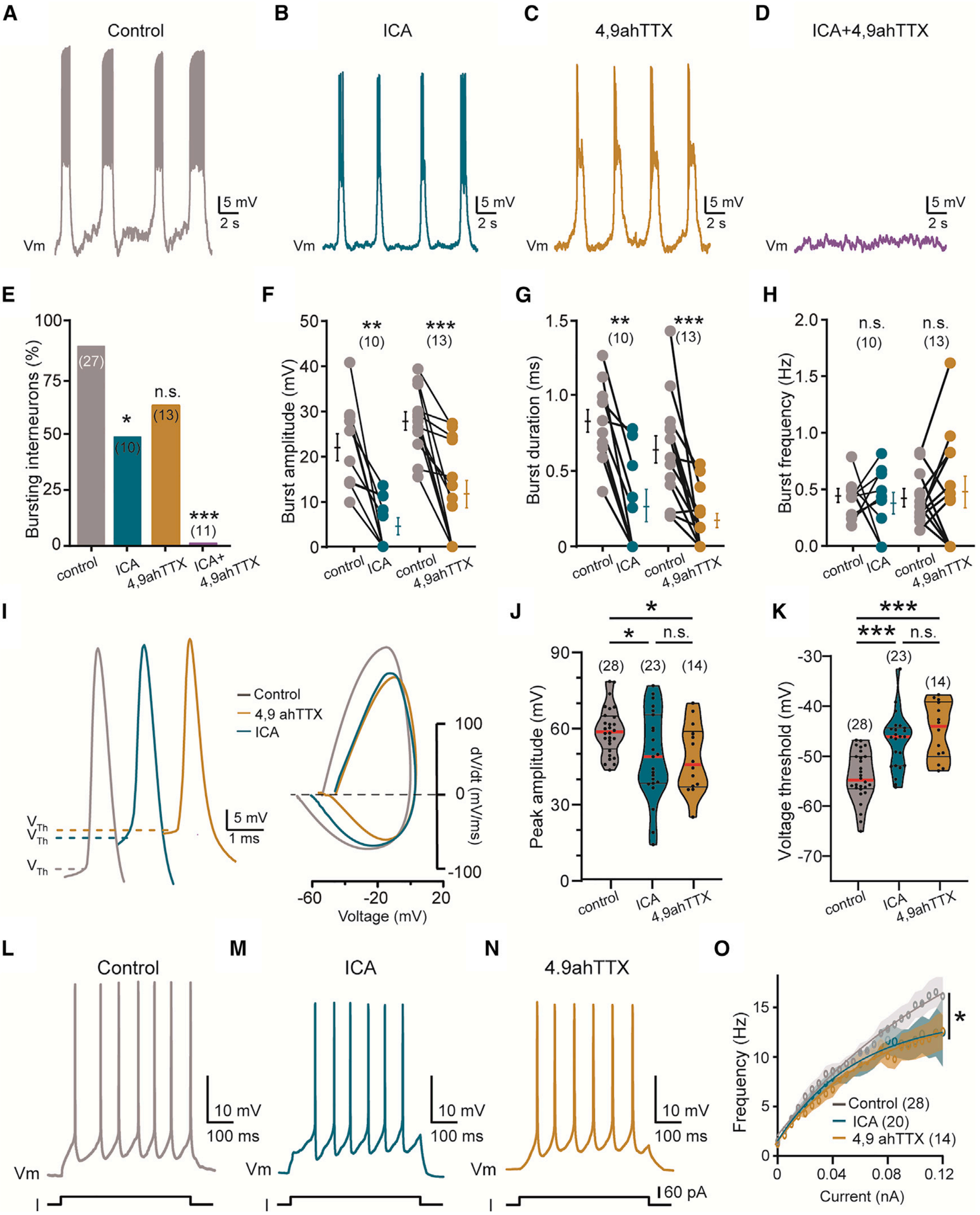

Figure 3. ***Nav1.6*** **channels work in tandem with** ***Nav1.1*** **channels for generating** $\boldsymbol{I_{NaP}}$**-dependent bursting properties**

(A–D) $[Ca^{2+}]_o$-free-saline-induced bursting activity recorded from ventromedial interneurons of the rhythmogenic CPG region (L_1–L_2) before (A, n = 7 mice) or during the bath application of ICA (B, 350 nM, n = 5 mice) or 4,9-ahTTX (C, 200 nM, n = 6 mice) or when the two drugs were coapplied (D, n = 7 mice).

(E) Quantification of the proportion of bursting cells (n = 10–27 cells).

(F–H) Quantification of burst parameters (n = 10–13 cells).

(I, L–N, and O) Voltage traces recorded from interneurons of the rhythmogenic CPG region in response to near-threshold (I) or incrementing (L–N) depolarizing pulses before (I and L, gray, n = 3 mice) or during the bath application of ICA (I and M, green, 350 nM, n = 3 mice) or 4,9-ahTTX (I and N, orange, 200 nM, *n* = 2 mice).

(I) Representative individual action potentials (left) with their phase plots (right) generated from the first derivative (dV/dt; y axis) versus membrane potential (mV; x axis). Dashed lines indicate the spiking threshold (V_{Th}). (J and K) Violin plots of the peak amplitude (J) and threshold (K) of the action potential (n = 14–28 cells). (O) Firing frequency as a function of the amplitude of the current pulse (n = 14–28 cells).

(legend continued on next page)

than the *Nav1.1* blocker (Figure 2F). Specifically, the spike was smaller and displayed a higher threshold (Figures 2G and 2H). Furthermore, ICA and 4,9-ahTTX lowered the firing rate (Figure 2I–2L). Notably, the *Nav1.6* blocker diminished the capacity to spike at high frequencies and led to a frank failure of the repetitive firing, not observed with ICA. The genetic deletion of *Nav1.1* or *Nav1.6* broadly recapitulated the distinct contributions of the two channels in firing properties of motoneurons, with only one-third of *Nav1.6*$^{-/-}$ motoneurons remaining bistable (Figure S4). In *Nav1.6*$^{-/-}$ motoneurons, the expression of *Nav1.1* was not restrained to the proximal part of the AIS like in wild type but was spread along the full length of the AIS (Figures S2C and S2D). The *Nav1.1* colocalized more extensively with PanNav in *Nav1.6*$^{-/-}$ than in wild-type motoneurons (Figure S2E). The compensation was independent of structural changes as the ankyrin-G expression pattern did not differ from wild type (Figure S1F). A similar compensation by *Nav1.6* did not occur in *Nav1.1*$^{-/-}$ motoneurons (Figures S2F–S2H).

Overall, these data indicate a critical role of *Nav1.6* channels in setting the excitability and firing properties of motoneurons, notably by supporting the self-sustained spiking activity that cannot be supported by *Nav1.1* channels.

Nav1.6 partnered with *Nav1.1* to generate bursting properties in interneurons

Most of interneurons (~90%) from the rhythmogenic CPG region displayed nonlinear firing properties manifested by bursting activities dependent on I_{NaP} and triggered by removing the extracellular Ca^{2+} (Figures 3A and 3E).[5,8] In nearly half of these interneurons, the pharmacological inhibition of either *Nav1.1* or *Nav1.6* abolished the bursting activity (Figure 3E). In the other half, the robustness of bursts decreased both in amplitude and duration without affecting the frequency (Figures 3B, 3C, and 3F–3H). The simultaneous application of the two blockers was required to abolish all bursting cells (Figures 3D and 3E). Similar results were obtained in locomotor-related Hb9 interneurons (Figures S5A–S5D). Bursting activities in *Nav1.1*$^{-/-}$ and *Nav1.6*$^{-/-}$ mice remained robust, comparable to those recorded in wild-type mice, but were abolished by 4,9-ahTTX and ICA, respectively (Figure S5E–S5J). In wild-type interneurons recorded in normal artificial cerebrospinal fluid (aCSF), the pharmacological inhibition of one of the two Nav channels equally decreased the amplitude of the spike and depolarized the threshold (Figures 3I–3K). Likewise, ICA and 4,9-ahTTX indistinguishably lowered the firing rate as the depolarizing current pulses increased (Figures 3L–3O). Smaller spikes were also observed both in *Nav1.1*$^{-/-}$ and *Nav1.6*$^{-/-}$ interneurons (Figures S5K and S5L). However, the higher voltage threshold and the lower firing rate were observed only in *Nav1.1*$^{-/-}$ interneurons (Figures S5K–S5Q). Once again, partial compensatory mechanisms occurred in *Nav1.6*$^{-/-}$ interneurons with the *Nav1.1* expression extended to the distal part of AIS (Figures S2I–S2K). Conversely, such homeostatic regulation by *Nav1.6* was not present in *Nav1.1*$^{-/-}$ interneurons (Figures S2L–S2N).

Together, these data show that both *Nav1.1* and *Nav.1.6* channels, ubiquitously expressed in the rhythmogenic CPG region, are partners and that they take an equivalent parts in regulating spiking properties and dynamics of oscillatory activities in interneurons.

I_{NaP} dominantly relies on *Nav1.6* in motoneurons and on the cooperative gating between *Nav1.1* and *Nav1.6* in interneurons

We here examined the contribution of the two Nav channels in the biophysical properties of I_{NaP}. In response to a slow ramp voltage, motoneurons and interneurons typically displayed a large inward voltage-dependent current attributable to I_{NaP} (Figures 4A and 4E; see also Tazerart et al.[8]). In motoneurons, the *Nav1.1* blocker ICA did not significantly alter I_{NaP} (Figures 4A–4D). By contrast, the *Nav1.6* blocker 4,9-ahTTX strongly decreased I_{NaP} in amplitude and shifted toward more depolarized values its voltage activation threshold without modifying the half-activation potential (Figures 4A–4D). The coapplication of 4,9-ahTTX and ICA abolished I_{NaP} (Figure 4B). Data were recapitulated in *Nav1.1*$^{-/-}$ and *Nav1.6*$^{-/-}$ motoneurons (Figures S6A–S6D), and the residual I_{NaP} was abolished by 4,9-ahTTX and ICA, respectively (Figures S6E–S6H). In interneurons, in the presence of either ICA or 4,9-ahTTX, the peak amplitude of I_{NaP} was mostly halved without affecting its activation threshold or the half-activation potential (Figures 4E–4H). Likewise, the coapplication of 4,9-ahTTX and ICA abolished I_{NaP} (Figure 4F). Astonishingly, biophysical properties of I_{NaP} in *Nav1.1*$^{-/-}$ and *Nav1.6*$^{-/-}$ interneurons were similar to wild-type littermates (Figures S6I–S6L), but it was almost inhibited by 4,9-ahTTX and ICA, respectively (Figure S6M–S6P).

These results further support the concept that I_{NaP} is dominantly mediated by *Nav1.6* in motoneurons and by the *Nav1.1*-*Nav1.6* partnership in interneurons.

Nav1.1 and *Nav1.6* channels participate in fictive locomotion

The presence of I_{NaP} at the level of the CPG is required for the locomotor rhythm generation in rodents.[4,5,7,8,12,13] Since the *Nav1.1-Nav1.6* partnership generates I_{NaP} in the rhythmogenic CPG region, we examined the role of the two channels in the operation of the locomotor rhythm-generating network by using whole-mount spinal cord preparation. During fictive locomotion, the bath application of ICA or 4,9-ahTTX on rhythm-generating networks decreased the locomotor burst amplitude without affecting temporal parameters of locomotor outputs (Figures 5A–5E). The coapplication of the two drugs strongly impaired locomotor outputs and ultimately led to them being abolished in most preparations (Figures 5F–5H). Note that the spinal cords isolated from *Nav1.1*$^{-/-}$ or *Nav1.6*$^{-/-}$ mice exhibited a quite normal locomotor-like activity (Figures S7A and S7B).

Numbers in brackets in (E)–(H), (J), (K), and (O) indicate the numbers of interneurons. Each dot in (J) and (K) represents an individual interneuron. Continuous lines in (O) represent best-fit functions for experimental data with 95% confidence interval. n.s., no significance; *$p < 0.05$; **$p < 0.01$; ***$p < 0.001$ (two-tailed Fisher test for E; two-tailed Wilcoxon paired test for F–H; one-way ANOVA with multiple comparisons for J and K; comparison of the fits for O). Error bars: mean ± SEM. See also Figure S5.

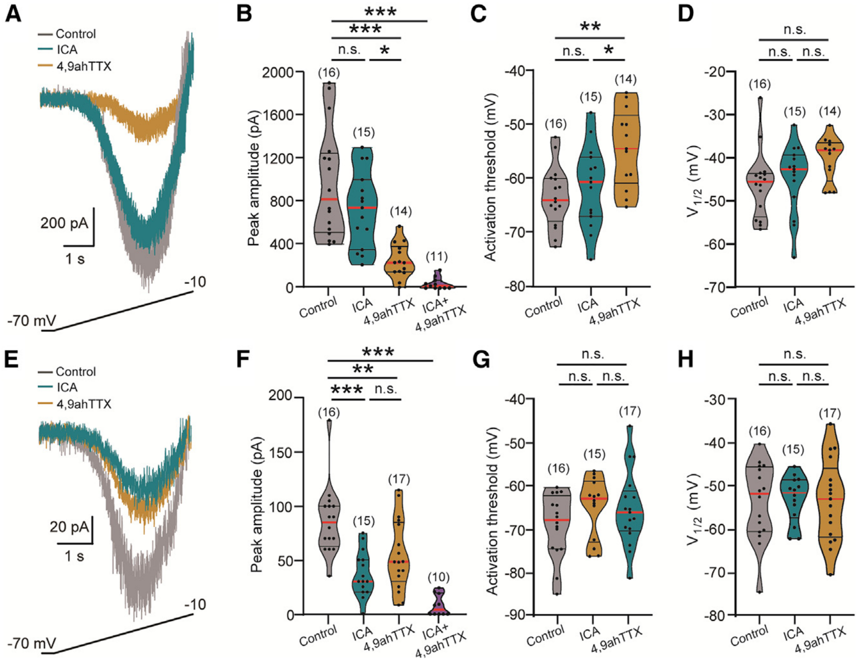

Figure 4. *Nav1.6* channels encode I_{NaP} in motoneurons

(A and E) Superimposed leak-subtracted I_{NaP} recorded from motoneurons (A) and interneurons of the rhythmogenic CPG region (E) in response to a slow ramping depolarization before (gray, n = 6 mice) and after the bath application of ICA (green, 350 nM, n = 4 mice) or 4,9-ahTTX (orange, 200 nM, n = 4 mice).

(B–D and F–H) Amplitude (B and F), threshold (C and G), and half-activation voltage (D and H) of I_{NaP} (n = 10–17 cells).

Numbers in brackets indicate the number of neurons. Each dot represents an individual neuron. n.s., no significance; $^{*}p < 0.05$; $^{**}p < 0.01$; $^{***}p < 0.001$ (one-way ANOVA with multiple comparisons).

See also Figure S6.

The recurrent recruitment of I_{NaP} in motoneurons has also been shown to increase the amplitude of the locomotor drive from the CPG.[12] To test the role of motoneuron *Nav1.1* and *Nav1.6* channels in the integration of rhythmic locomotor inputs, we applied drugs to motoneuron pools caudally located (Figures 5I and 5J). The *Nav1.1* blocker ICA did not affect fictive locomotor outputs (Figures 5K and 5M). By contrast, the *Nav1.6* blocker 4,9-ahTTX strongly decreased the amplitude, duration, and regularity of locomotor outputs without affecting the cycle period (Figures 5L and 5M). Note that these effects were observed without noticeable alterations of locomotor outputs recorded at the CPG level spared from blockers by the Vaseline barrier (Figures S7C–S7F).

Together, these data indicate that *Nav1.1* and *Nav1.6* taken individually are not essential for the locomotor rhythm generation but that they work in tandem at the level of the CPG to ensure rhythmogenesis. Our findings also suggest that *Nav1.6* channels are rhythmically activated in motoneurons to amplify locomotor outputs.

Silencing *Nav1.6* in spinal motoneurons disturbs motor behaviors

To specifically discriminate the behavioral role of *Nav1.6* in spinal motoneurons, we injected the adeno-associated virus serotype 2 retrograde (AAV2-retro) encoding the *Nav1.6*-shRNA with a green fluorescent reporter (EGFP) into the *triceps surae* muscle of neonatal mice. The AAV2-retro was previously shown to high-efficiently, extensively, and bilaterally transduce most of lumbar motoneurons after the unilateral intramuscular injection in neonatal mice.[39] Note that the following analyses are not exclusively focused on the *triceps surae* motoneurons, as the viral vector transfects all the motoneurons indiscriminately. As early as the 2nd week post-injection, the expression of EGFP was observed in ventral horns of the spinal cord from T7–T11 to S1–S3, and 46.8% ± 8.8% of lumbar motoneurons (533 out of 1,169 large cholinergic neurons in the L3–L5 ventral horns from 3 mice) were transduced (Figure 6A). Concomitantly, the viral transfection led to a decrease of the membrane protein expression of sodium channels in the lumbar spinal cord by ~28% (Figure 6B). The weak fixation condition required for immunostaining *Nav1.6* channels is not sufficient to retain the cytosolic GFP reporter from transduced cells. Despite this constraint, we observed that one-third (35%) of lumbar motoneurons no longer expressed *Nav1.6* at the AIS (Figures 6C–6F). Compared with motoneurons transduced with the scramble short hairpin RNA (shRNA), the proportion of bistable motoneurons markedly decreased to ~23% in *Nav1.6*-shRNA mice (Figures 6G–6I) with a significant decrease of I_{NaP} amplitude without modifying the activation threshold (Figure 6J–6L). The amplitude of the spike and firing rates also decreased without affecting the spike threshold or the excitability of motoneurons (Figures S4M–S4S).

Mice transduced with *Nav1.6*-shRNA can be phenotypically distinguished from control-shRNA mice as early as the 2nd week post-injection. At rest, *Nav1.6*-shRNA mice typically showed a wider base of support, with hind paws pointed outward and visible outside the body contour (Figure 7A). Besides having reduced hind paw print areas (Figure 7B), *Nav1.6*-shRNA mice showed striking locomotor deficits as they failed to adapt to accelerated speed in the rotarod test (Figure 7C). These locomotor deficits did not fade over weeks and persisted in young (4-week-old) adult mice (Figure 7C). At this age, our data indicate that temporal parameters of the stepping movements were normal in *Nav1.6*-shRNA mice, with animals walking with a regular and alternating locomotor pattern, although with a wider base of support (Figure 7D). However, *Nav1.6*-shRNA mice stereotypically walked with a markedly collapsed basin (Figure 7E; Videos S1 and S2). Kinematic reconstruction of hindlimb movements revealed that hip and knee joint angles from *Nav1.6*-shRNA mice were ~10° less extended throughout the stance

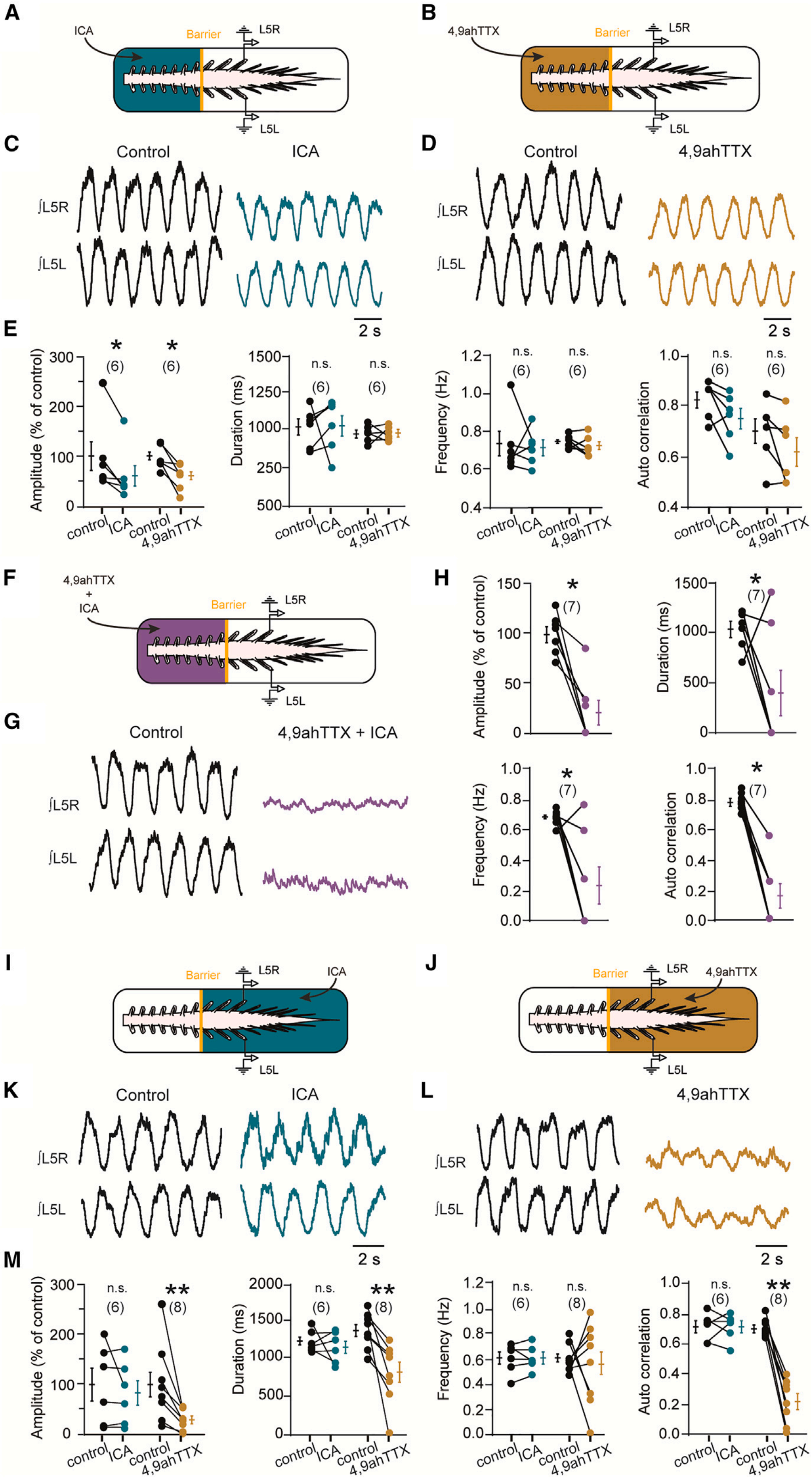

(legend on next page)

phase, while ankle joint angles remained similar to control-shRNA mice (Figures 7F and 7G). No significant differences were observed in kinematic variables during the swing phase (Figures 7F and 7G).

Altogether, these data provide evidence that *Nav1.6,* as the molecular constituent of I_{NaP} in lumbar motoneurons, is critical in promoting self-sustained spiking activity and plays a key role in producing an efficient postural tone in hindlimbs.

DISCUSSION

The study provides important insights into how the spinal locomotor network operates: (1) it shows that *Nav1.6* works in tandem with *Nav1.1* in CPG interneurons to generate I_{NaP} bursting and thereby the locomotor rhythm, (2) it identifies *Nav1.6* as the main molecular player for I_{NaP} in bistable motoneurons to promote a self-sustained spiking activity, and (3) it assigns to motoneuronal *Nav1.6* channels behavioral roles in producing a postural tone and amplifying the locomotor output.

In our study, the distinct localization of *Nav1.1* and *Nav1.6* channels along the AIS resonates with earlier observations in the spinal cord.[40,41] This specific spatial organization of sodium channel isoforms, evident in multiple brain regions, is believed to modulate neuronal excitability and firing dynamics, facilitating accurate temporal encoding and information processing.[42,43] We identified *Nav1.1* and *Nav1.6* as the molecular determinants for most of the I_{NaP} within the spinal locomotor network. If *Nav1.1* and *Nav1.6* conduct I_{NaP} in the rhythmogenic CPG region, *Nav1.6* makes a larger contribution to I_{NaP} in motoneurons. This agrees with the predominant expression of *Nav1.6* in the AIS of motoneurons, supposed to be the primary source of I_{NaP}.[44] As also found in supraspinal structures,[45–49] *Nav1.6* controls the excitability of spinal neurons by hyperpolarizing the spike threshold. The I_{NaP} hyperpolarizes the spike threshold both in motoneurons and CPG interneurons.[13] Since *Nav1.6* singularly mediates I_{NaP},[47,50–60] it might be assumed that the persistent *Nav1.6* current regulates neuronal excitability by lowering the spike threshold, especially in motoneurons.[61]

In vertebrates, I_{NaP} functions as the primary mechanism to produce the locomotor rhythm,[7] and we here show that *Nav1.1* and *Nav1.6* cooperate to mediate I_{NaP} within the rhythmogenic CPG region. Both are sufficient for rhythmogenesis, but the combination of the two is required for a robust locomotor rhythm. When applied over the caudal-most lumbar segments, the *Nav1.6* blocker 4,9-ahTTX reduces locomotor outputs similarly to the I_{NaP} blocker riluzole.[12,13] It is thus believed that the persistent *Nav1.6* current in motoneurons potentiates synaptic drives from the CPG to amplify locomotor outputs. This is highly plausible considering the role of I_{NaP} membrane oscillation amplification in motoneurons[9] and in initiating spikes during locomotor-like inputs.[62] As fast walking is more difficult without *Nav1.6* in motoneurons, such mechanisms appear critical for highly demanding locomotor tasks. It is conceivable that the recruitment of *Nav1.6* channels in motoneurons rises with the speed of locomotion, amplifying drives from the CPG to produce forceful motor outputs.

The acute pharmacological inhibition of Nav channels differs qualitatively from the chronic deletion in genetic models. Specifically, the striking robustness of both bursting cells and the locomotor rhythm in mutant mice suggests long-term compensatory mechanisms. A shift from Na^+- to Ca^{2+}-dependent mechanism of bursting reported in *Nav1.6*$^{-/-}$ Purkinje neurons[63] is unlikely in our Ca^{2+}-free recording solution. A reciprocal homeostatic expression between Nav channel isoforms may contribute[55,56,64,65] but does not appear as the main factor in our study. An alternative mechanism might involve a lower recruitment of K^+ currents in response to the decrease of the Na^+ conductance.[46,63] This hypothesis appears to be the most likely since rhythmogenesis of the CPG relies on dynamic interactions between I_{NaP} and the M-current mediated by *Kv7.2* channels.[10] Because *Kv7.2* channels are coexpressed with Nav channels in CPG interneurons,[10] we posit that *Nav1.1* and *Nav1.6* are key partners of *Kv7.2* in regulating responsiveness of locomotor-related bursting cells.

Our finding shows *Nav1.6* as a key player of the bistability in motoneurons, while *Nav1.1* channels have a secondary role. The reduction in self-sustained spiking activity may be due to the unique biophysical properties of *Nav1.6*, which exhibits a use-dependent potentiation during a long-lasting discharge.[66] This behavior is in contrast to *Nav1.1*, which becomes inactivated under similar conditions.[67] Once again, we posit the persistent *Nav1.6* current component as critical. This assumption follows earlier studies where bistable motoneurons disappear with the I_{NaP} blocker riluzole,[17,18,21] irrespective of the spike threshold shift induced by riluzole.[13,62,68,69] Therefore, the substantial drop in I_{NaP} following the deletion of *Nav1.6* offers a biophysical basis for the lower capacity of motoneurons to spike tonically. Collectively, a scenario arises where the persistent *Nav1.6* current leads to a mechanism of self-maintaining motoneuronal output as follow: secondary to the recruitment of Ca^{2+} channels during repetitive spikes, *Nav1.6*-mediated I_{NaP} indirectly fuels motoneurons in Ca^{2+} to activate Trpm5 channels governing a plateau potential responsible for the self-sustained

Figure 5. *Nav1.1* and *Nav1.6* channels participate in fictive locomotion

(A, B, F, I, and J) Schematic representation of the whole-mount spinal cord with the recording glass electrodes from the lumbar segment L_5 (L_5R/L). The yellow solid line represents the Vaseline barrier. Built at the L_2/L_3 level, the Vaseline barrier allows the selective application of drugs over the rostral (A, B, and F, above the L_3 segment) or the caudal lumbar segments (I and J, below L_3 segment).

(C, D, G, K, and L) Ventral-root recordings of NMA/5-HT-induced fictive locomotor activity before and after adding ICA (C and K, 350 nM, n = 12 mice) or 4,9-ahTTX (D and L, 200 nM, n = 14 mice) or the two drugs (G, n = 7 mice) to rostral (C, D, and G) or caudal (K and L) lumbar segments.

(E, H, and M) Quantification of locomotor burst parameters.

Numbers in brackets in (E), (H), and (M) indicate the number of spinal cords. n.s., no significance; $^*p < 0.05$; $^{**}p < 0.01$ (two-tailed Wilcoxon paired test for E, H, and M). Error bars: mean ± SEM.

See also Figure S7.

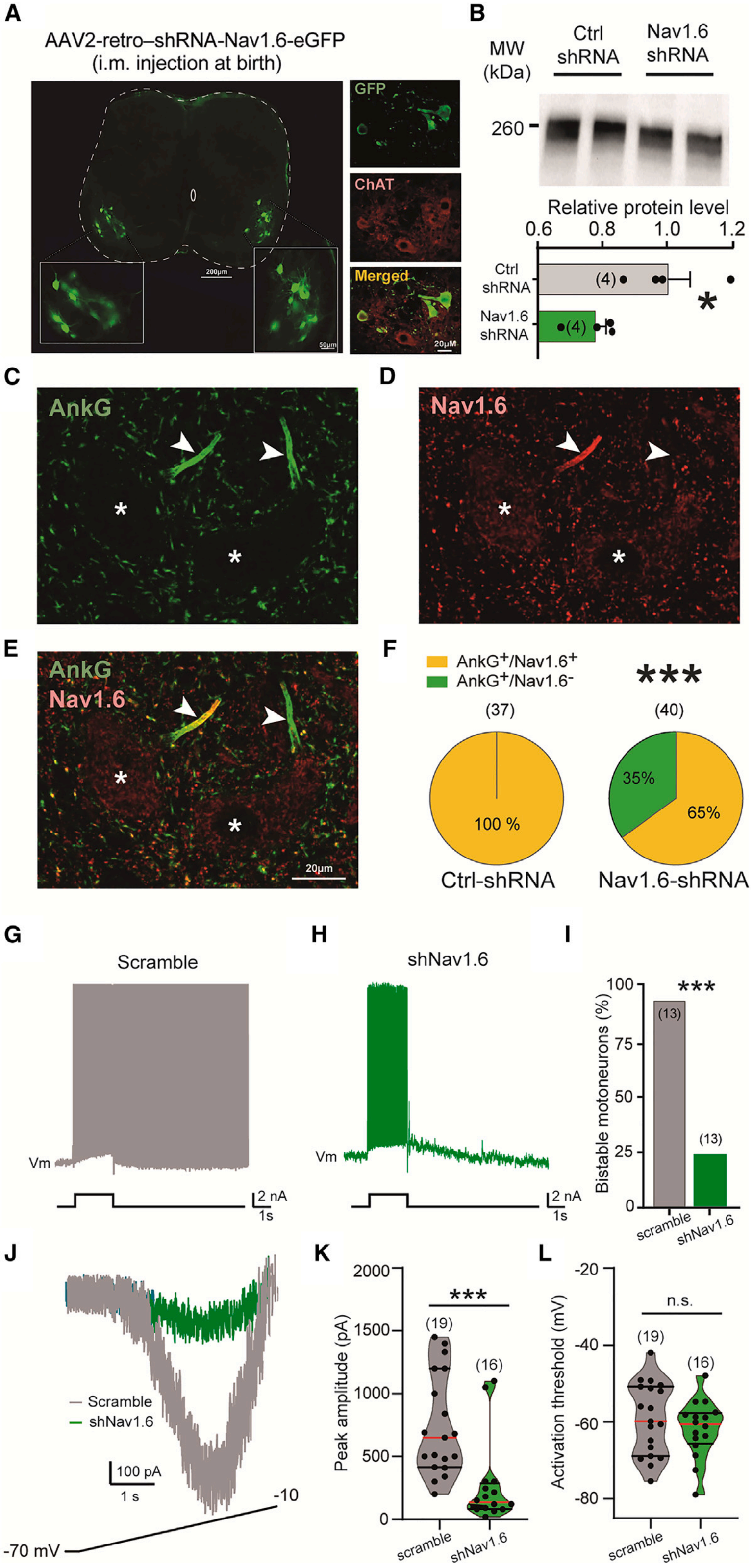

Figure 6. Silencing *Nav1.6* channels in spinal motoneurons impairs I_{NaP} and the self-sustained spiking activity

(A) Left: native GFP-expressing motoneurons visualized in the lumbar spinal cord from a postnatal day 10 (P10) mouse and transduced by the AAV2-retro-shRNA-*Nav1.6*-EGFP injected into the *triceps surae* muscle at birth. Scale bar represents 200 μm. Insets are high magnifications of the ventral horn showing native GFP-expressing motoneurons. Scale bar represents 50 μm. Right: high magnification of the ventral horn showing native fluorescence of motoneurons transduced by AAV2-retro (top) and immunostained for choline acetyltransferase (middle, ChAT antibody; bottom, merged images).

(B) Top: PanNav immunoblots of lumbar segments from P10 mice intramuscularly injected at birth with the AAV2-retro encoding either a scramble shRNA (n = 4 mice) or a *Nav1.6*-targeting shRNA (n = 4 mice). One mouse per lane. Bottom: group means quantification of the ∼260 kDa band normalized to scramble-injected controls.

(C–E) Representative single optical sections showing immunostaining against ankyrin-G (C) and *Nav1.6* (D) expressed in AISs of motoneurons from a P14 mouse transduced by the *Nav1.6*-targeting shRNA; merge image in (E). Asterisks indicate the motoneuron nucleus position and arrows AISs. Scale bars represent 20 μm.

(F) Proportion of motoneurons double labeled with ankyrin-G and *Nav1.6* antibodies in mice transduced with the scramble shRNA (left, n = 37 cells from 3 mice) or with the *Nav1.6*-shRNA (right, n = 40 cells from 3 mice).

(G and H) Voltage traces in response to suprathreshold depolarizing pulse and recorded from EGFP+ motoneurons transduced either with the scramble (G, gray, n = 3 mice) or with the *Nav1.6*-targeting shRNA (H, green, n = 4 mice).

(I) Group mean quantification of the proportion of bistable motoneurons (n = 13 cells).

(J) Superimposed leak-subtracted I_{NaP} recorded in response to a slow ramping depolarization from EGFP+ motoneurons transduced either with the scramble (gray, n = 2 mice) or with the *Nav1.6*-targeting shRNA (green, n = 2 mice).

(K and L) Violin plots of the peak amplitude (K) and voltage threshold (L) of I_{NaP} (n = 16–19 cells).

Numbers in brackets in (F), (I), (K), and (L) indicate the numbers of motoneurons. Each circle represents an individual motoneuron. n.s., no significance; $^{*}p < 0.05$; $^{***}p < 0.001$ (two-tailed Mann-Whitney test for B, K, and L; two-tailed Fisher test for F and I). Error bars: mean ± SEM.

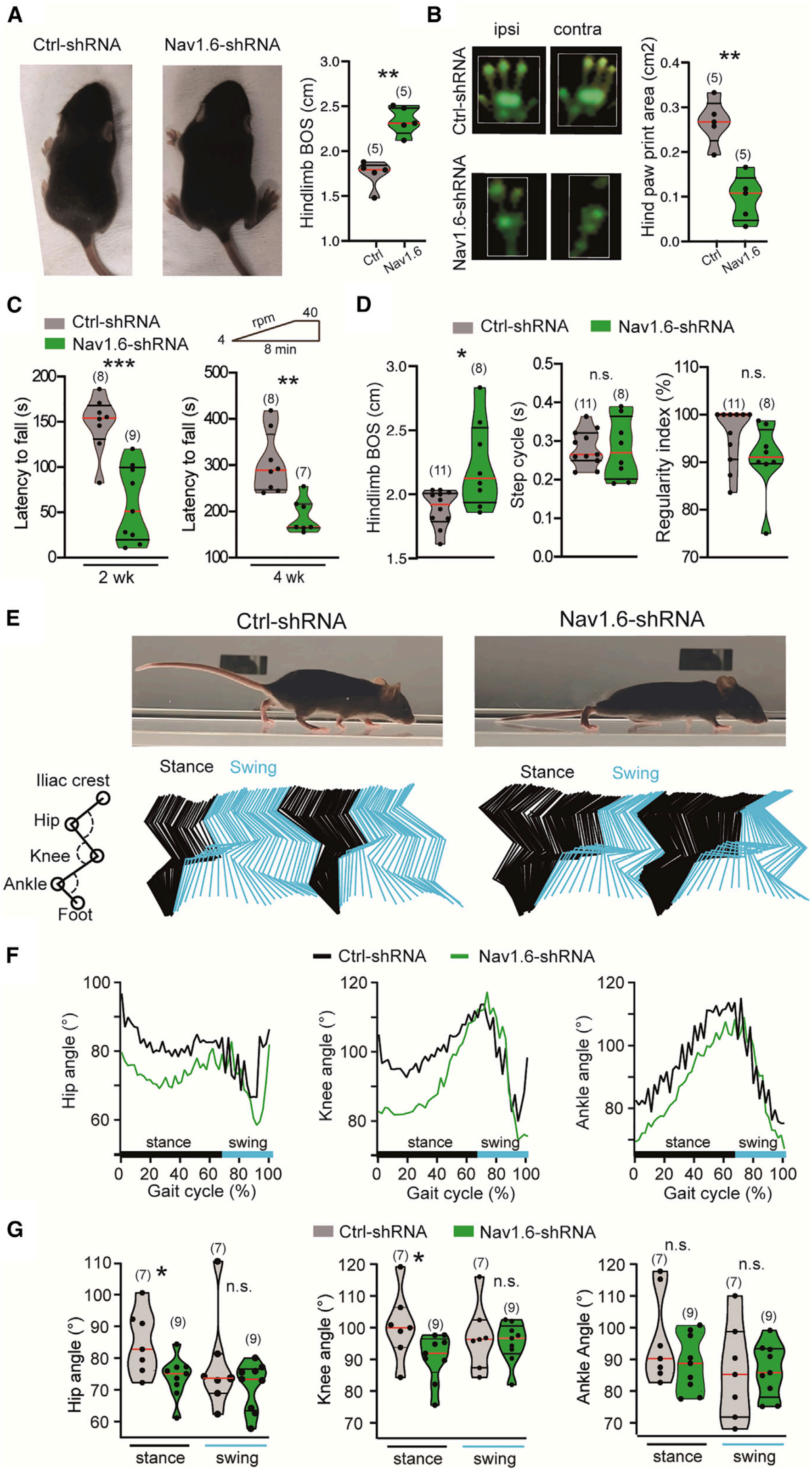

(legend on next page)

spiking.[17,20] By virtue of this recruitment cascade, *Nav1.6* channels serve as the gateway to self-sustained spiking allowing efficient postural tone in muscles.

Nav1.6 is expressed throughout the nervous system but not in muscles.[29,31,70,71] Its global deletion develops ataxia and tremors of hindlimbs progressing to paralysis.[72] The disrupted function of the motor system likely involves central motor control impairments but not that of the CPG for locomotion since it operates normally in *Nav1.6*$^{-/-}$ mice (Figures S7A and S7B). The selective inactivation of *Nav1.6* in cerebellar Purkinje neurons results in ataxia and tremor symptoms without paresis of hindlimbs.[48] Here, the selective loss of *Nav1.6* in a large proportion of lumbar motoneurons decreases the hindlimb postural tone without ataxia or tremors. Then, the neurological disorders of *Nav1.6*$^{-/-}$ mice can be decoupled and respectively attributed to distinct alterations in cerebellar (ataxia, tremor) and spinal (paresis of hindlimbs) neurons. We recently related the postural tone deficit to a decrease in the ability of motoneurons to produce a self-sustained spiking.[20] From the present study, a straightforward conclusion is that *Nav1.6* supports most of the native I_{NaP} involved in promoting self-sustained spiking activity in bistable motoneurons. Therefore, the postural deficit after deleting or silencing *Nav1.6* channels can be considered a direct consequence of the loss of bistable motoneurons. According to a cell-type-dependent expression of sodium channels,[73] a heterogeneous role of *Nav1.6* channels throughout the motoneuronal population might explain the proximodistal gradient motor deficit observed in *Nav1.6*-shRNA mice, reminiscent of the proximal muscle weakness reported in *Nav1.6*$^{-/-}$ mice.[74]

Overall, this study provides insights into the operation of the locomotor network whereby *Nav1.1* and *Nav1.6* represent a functional set of voltage-gated sodium channels that endow the locomotor CPG with rhythmogenic properties, whereas a powerful motor output during locomotion is associated with the cyclic activation of *Nav1.6* channels in motoneurons. It also brings clear support to a specific behavioral role of *Nav1.6* in motoneurons in controlling the postural tone by providing I_{NaP}-dependent bistable properties.

Limitations of the study

Our study provides valuable insights into the roles of *Nav1.1* and *Nav1.6* within the spinal locomotor network. However, some limitations warrant consideration. Primarily, by focusing on *Nav1.1* and *Nav1.6*, we may have overlooked the potential contributions of other ion channels or molecular components, notably β subunits, which could play a pivotal role in regulating I_{NaP}. Additionally, the *in vitro* conditions, especially the use of a Ca^{2+}-free recording solution, may not accurately mirror the complexities of the *in vivo* environment, potentially influencing the neuronal behaviors observed. A significant constraint is that our experiments were predominantly conducted on young animals still undergoing developmental processes, raising questions about the applicability of our findings to mature, adult animals. To achieve a comprehensive understanding of the spinal locomotor network and its multifaceted functions, future research should address and expand upon these limitations.

STAR★METHODS

Detailed methods are provided in the online version of this paper and include the following:

- KEY RESOURCES TABLE
- RESOURCE AVAILABILITY
    - ○ Lead contact
    - ○ Materials availability
    - ○ Data and code availability
- EXPERIMENTAL MODEL AND SUBJECT DETAILS
    - ○ Mice
- METHOD DETAILS
    - ○ shRNA construct
    - ○ Intramuscular vector delivery
    - ○ *In vitro* preparations
    - ○ Assessment of motor behaviors
    - ○ Immunostaining
    - ○ Nav channels protein quantification
- QUANTIFICATION AND STATISTICAL ANALYSIS
    - ○ Data analysis
    - ○ Statistics

SUPPLEMENTAL INFORMATION

Supplemental information can be found online at https://doi.org/10.1016/j.celrep.2023.113085.

Figure 7. Silencing *Nav1.6* in lumbar motoneurons disturbs motor behaviors

(A) Left and middle: top views of 2-week-old wild-type mice transduced either with the scramble shRNA (left) or with the *Nav1.6*-shRNA (middle). Right: violin plots of the base of support at rest (n = 5 mice).

(B) Left: typical hind paw prints captured by the CatWalk XT automated gait analysis system from 2-week-old wild-type mice either transduced with the scramble shRNA (top) or with the *Nav1.6*-shRNA (bottom). Right: violin plots of the hind paw print area (n = 5 mice).

(C) Violin plots of the latency to fall from a rod rotating at accelerated speed (4–40 rpm). The mice (n = 7–9 mice) were stratified into two age groups: 2- and 4-week-old mice.

(D) Violin plots of the base of support (left), step cycle (middle), and regularity index of paw placements (right) during CatWalk locomotion from 4-week-old mice (n = 8–11).

(E) Side view of 4-week-old wild-type mice freely walking through a corridor on a glass walkway and transduced either with the scramble shRNA (left, n = 7 mice) or with the *Nav1.6*-shRNA (right, n = 9 mice). Bottom: color-coded stick decomposition of hindlimb movement during two consecutive steps.

(F) Angular excursion of three joints (hip, knee, and ankle) during the locomotor cycle.

(G) Decoding performance for three joint angles (mean θ of the hip, knee, and ankle) during the stance and swing phases.

Numbers in brackets indicate the number of mice. Each circle represents an individual mouse. n.s., no significance; *$p < 0.05$; **$p < 0.01$; ***$p < 0.001$ (two-tailed Mann–Whitney test for A–D and G).

See also Videos S1 and S2.

ACKNOWLEDGMENTS

We are grateful to Jérémy Verneuil for coding videos, Hélène Bras for technical advice on the administration of the viral vector, Jean-Charles Viemari for his assistance in fictive locomotor experiments, and Geneviève Rougon and Nejada Dingu for their valuable input to the manuscript. This research was supported by Agence National de la Recherche Scientifique (SpasT-SCI-T, ANR-21-CE17-0060 to F.B.) and the French Institut pour la Recherche sur la Moelle épinière et l'Encéphale (to F.B.).

AUTHOR CONTRIBUTIONS

B.D. designed, performed, and analyzed most of *in vitro* and *in vivo* experiments and wrote the first draft of the manuscript. C.B. designed, performed, and analyzed immunohistochemistry and biochemistry experiments. S.Z. and R.B. designed and performed some of the *in vitro* experiments. F.B. conceptualized, administrated, designed, supervised, and funded the whole project, performed and analyzed some *in vitro* experiments, and wrote the manuscript.

DECLARATION OF INTERESTS

The authors declare no competing interests.

INCLUSION AND DIVERSITY

We support inclusive, diverse, and equitable conduct of research.

Received: April 10, 2023
Revised: June 29, 2023
Accepted: August 16, 2023

REFERENCES

1. Kiehn, O. (2016). Decoding the organization of spinal circuits that control locomotion. Nat. Rev. Neurosci. *17*, 224–238. https://doi.org/10.1038/nrn.2016.9.
2. Grillner, S., and El Manira, A. (2020). Current Principles of Motor Control, with Special Reference to Vertebrate Locomotion. Physiol. Rev. *100*, 271–320. https://doi.org/10.1152/physrev.00015.2019.
3. Del Negro, C.A., Funk, G.D., and Feldman, J.L. (2018). Breathing matters. Nat. Rev. Neurosci. *19*, 351–367. https://doi.org/10.1038/s41583-018-0003-6.
4. Brocard, F., Tazerart, S., and Vinay, L. (2010). Do pacemakers drive the central pattern generator for locomotion in mammals? Neuroscientist *16*, 139–155.
5. Brocard, F., Shevtsova, N.A., Bouhadfane, M., Tazerart, S., Heinemann, U., Rybak, I.A., and Vinay, L. (2013). Activity-dependent changes in extracellular ca(2+) and k(+) reveal pacemakers in the spinal locomotor-related network. Neuron *77*, 1047–1054.
6. Song, J., Pallucchi, I., Ausborn, J., Ampatzis, K., Bertuzzi, M., Fontanel, P., Picton, L.D., and El Manira, A. (2020). Multiple Rhythm-Generating Circuits Act in Tandem with Pacemaker Properties to Control the Start and Speed of Locomotion. Neuron *105*, 1048–1061.e4. https://doi.org/10.1016/j.neuron.2019.12.030.
7. Brocard, F. (2019). New channel lineup in spinal circuits governing locomotion. Current opinion in Physiology *8*, 14–22. https://doi.org/10.1016/j.cophys.2018.11.009.
8. Tazerart, S., Vinay, L., and Brocard, F. (2008). The persistent sodium current generates pacemaker activities in the central pattern generator for locomotion and regulates the locomotor rhythm. J. Neurosci. *28*, 8577–8589.
9. Ziskind-Conhaim, L., Wu, L., and Wiesner, E.P. (2008). Persistent sodium current contributes to induced voltage oscillations in locomotor-related hb9 interneurons in the mouse spinal cord. J. Neurophysiol. *100*, 2254–2264.
10. Verneuil, J., Brocard, C., Trouplin, V., Villard, L., Peyronnet-Roux, J., and Brocard, F. (2020). The M-current works in tandem with the persistent sodium current to set the speed of locomotion. PLoS Biol. *18*, e3000738. https://doi.org/10.1371/journal.pbio.3000738.
11. Rancic, V., and Gosgnach, S. (2021). Recent Insights into the Rhythmogenic Core of the Locomotor CPG. Int. J. Mol. Sci. *22*, 1394. https://doi.org/10.3390/ijms22031394.
12. Tazerart, S., Viemari, J.C., Darbon, P., Vinay, L., and Brocard, F. (2007). Contribution of Persistent Sodium Current to Locomotor Pattern Generation in Neonatal Rats. J. Neurophysiol. *98*, 613–628.
13. Zhong, G., masino, M.A., and Harris-Warrick, R.M. (2007). Persistent sodium currents participate in fictive locomotion generation in neonatal mouse spinal cord. J. Neurosci. *27*, 4507–4518.
14. Ryczko, D., Charrier, V., Ijspeert, A., and Cabelguen, J.M. (2010). Segmental oscillators in axial motor circuits of the salamander: distribution and bursting mechanisms. J. Neurophysiol. *104*, 2677–2692.
15. Tong, H., and McDearmid, J.R. (2012). Pacemaker and plateau potentials shape output of a developing locomotor network. Curr. Biol. *22*, 2285–2293. https://doi.org/10.1016/j.cub.2012.10.025.
16. Svensson, E., Jeffreys, H., and Li, W.C. (2017). The modulation of two motor behaviors by persistent sodium currents in Xenopus laevis tadpoles. J. Neurophysiol. *118*, 121–130. https://doi.org/10.1152/jn.00755.2016.
17. Bouhadfane, M., Tazerart, S., Moqrich, A., Vinay, L., and Brocard, F. (2013). Sodium-mediated plateau potentials in lumbar motoneurons of neonatal rats. J. Neurosci. *33*, 15626–15641.
18. Harvey, P.J., Li, Y., Li, X., and Bennett, D.J. (2005). Persistent sodium currents and repetitive firing in motoneurons of the sacrocaudal spinal cord of adult rats. J. Neurophysiol. 00335.
19. Li, Y., Gorassini, M.A., and Bennett, D.J. (2004). Role of persistent sodium and calcium currents in motoneuron firing and spasticity in chronic spinal rats. J. Neurophysiol. *91*, 767–783.
20. Bos, R., Drouillas, B., Bouhadfane, M., Pecchi, E., Trouplin, V., Korogod, S.M., and Brocard, F. (2021). Trpm5 channels encode bistability of spinal motoneurons and ensure motor control of hindlimbs in mice. Nat. Commun. *12*, 6815. https://doi.org/10.1038/s41467-021-27113-x.
21. Brocard, C., Plantier, V., Boulenguez, P., Liabeuf, S., Bouhadfane, M., Viallat-lieutaud, A., Vinay, L., and Brocard, F. (2016). Cleavage of Na(+) channels by calpain increases persistent Na(+) current and promotes spasticity after spinal cord injury. Nat. Med. *22*, 404–411. https://doi.org/10.1038/nm.4061.
22. Plantier, V., and Brocard, F. (2017). [Calpain as a new therapeutic target for treating spasticity after a spinal cord injury]. Med. Sci. *33*, 629–636. https://doi.org/10.1051/medsci/20173306020.
23. Bories, C., Amendola, J., Lamotte d'Incamps, B., and Durand, J. (2007). Early electrophysiological abnormalities in lumbar motoneurons in a transgenic mouse model of amyotrophic lateral sclerosis. Eur. J. Neurosci. *25*, 451–459. https://doi.org/10.1111/j.1460-9568.2007.05306.x.
24. Delestrée, N., Manuel, M., Iglesias, C., ElBasiouny, S.M., Heckman, C.J., and Zytnicki, D. (2014). Adult spinal motoneurones are not hyperexcitable in a mouse model of inherited amyotrophic lateral sclerosis. J. Physiol. *592*, 1687–1703. https://doi.org/10.1113/jphysiol.2013.265843.
25. Martínez-Silva, M.d.L., Imhoff-Manuel, R.D., Sharma, A., Heckman, C.J., Shneider, N.A., Roselli, F., Zytnicki, D., and Manuel, M. (2018). Hypoexcitability precedes denervation in the large fast-contracting motor units in two unrelated mouse models of ALS. Elife *7*, 30955. https://doi.org/10.7554/eLife.30955.
26. Maingret, F., Coste, B., Padilla, F., Clerc, N., Crest, M., Korogod, S.M., Delmas, P., Korogod, S.M., Osorio, N., Kulagina, I.B., and Delmas, P. (2008). Inflammatory mediators increase Nav1.9 current and excitability in nociceptors through a coincident detection mechanism. J. Gen. Physiol. *131*, 211–225. https://doi.org/10.4161/19336950.2014.973784.

27. Plantier, V., Sanchez-Brualla, I., Dingu, N., Brocard, C., Liabeuf, S., Gackière, F., and Brocard, F. (2019). Calpain fosters the hyperexcitability of motoneurons after spinal cord injury and leads to spasticity. Elife *8*, e51404. https://doi.org/10.7554/eLife.51404.

28. Vacher, H., Mohapatra, D.P., and Trimmer, J.S. (2008). Localization and targeting of voltage-dependent ion channels in mammalian central neurons. Physiol. Rev. *88*, 1407–1447. https://doi.org/10.1152/physrev.00002.2008.

29. Schaller, K.L., Krzemien, D.M., Yarowsky, P.J., Krueger, B.K., and Caldwell, J.H. (1995). A novel, abundant sodium channel expressed in neurons and glia. J. Neurosci. *15*, 3231–3242.

30. Fukuoka, T., Kobayashi, K., and Noguchi, K. (2010). Laminae-specific distribution of alpha-subunits of voltage-gated sodium channels in the adult rat spinal cord. Neuroscience *169*, 994–1006. https://doi.org/10.1016/j.neuroscience.2010.05.058.

31. Felts, P.A., Yokoyama, S., Dib-Hajj, S., Black, J.A., and Waxman, S.G. (1997). Sodium channel [alpha]-subunit mRNAs I, II, III, NaG, Na6 and hNE (PN1): different expression patterns in developing rat nervous system. Brain Res. Mol. Brain Res. *45*, 71–82.

32. Westenbroek, R.E., Merrick, D.K., and Catterall, W.A. (1989). Differential subcellular localization of the RI and RII Na+ channel subtypes in central neurons. Neuron *3*, 695–704. https://doi.org/10.1016/0896-6273(89)90238-9.

33. Jarnot, M., and Corbett, A.M. (2006). Immunolocalization of NaV1.2 channel subtypes in rat and cat brain and spinal cord with high affinity antibodies. Brain Res. *1107*, 1–12. https://doi.org/10.1016/j.brainres.2006.05.090.

34. Cazalets, J.R., Borde, M., and Clarac, F. (1995). Localization and organization of the central pattern generator for hindlimb locomotion in newborn rat. J. Neurosci. *15*, 4943–4951.

35. Kjaerulff, O., and Kiehn, O. (1996). Distribution of Networks Generating and Coordinating Locomotor Activity in the Neonatal Rat Spinal Cord In Vitro: A Lesion Study. J. Neurosci. *16*, 5777–5794.

36. Rosker, C., Lohberger, B., Hofer, D., Steinecker, B., Quasthoff, S., and Schreibmayer, W. (2007). The TTX metabolite 4,9-anhydro-TTX is a highly specific blocker of the Na(v1.6) voltage-dependent sodium channel. Am. J. Physiol. Cell Physiol. *293*, C783–C789.

37. Osteen, J.D., Sampson, K., Iyer, V., Julius, D., and Bosmans, F. (2017). Pharmacology of the Nav1.1 domain IV voltage sensor reveals coupling between inactivation gating processes. Proc. Natl. Acad. Sci. USA *114*, 6836–6841. https://doi.org/10.1073/pnas.1621263114.

38. Griffith, T.N., Docter, T.A., and Lumpkin, E.A. (2019). Tetrodotoxin-Sensitive Sodium Channels Mediate Action Potential Firing and Excitability in Menthol-Sensitive Vglut3-Lineage Sensory Neurons. J. Neurosci. *39*, 7086–7101. https://doi.org/10.1523/JNEUROSCI.2817-18.2019.

39. Chen, Z., Fan, G., Li, A., Yuan, J., and Xu, T. (2020). rAAV2-Retro Enables Extensive and High-Efficient Transduction of Lower Motor Neurons following Intramuscular Injection. Mol. Ther. Methods Clin. Dev. *17*, 21–33. https://doi.org/10.1016/j.omtm.2019.11.006.

40. Duflocq, A., Chareyre, F., Giovannini, M., Couraud, F., and Davenne, M. (2011). Characterization of the axon initial segment (AIS) of motor neurons and identification of a para-AIS and a juxtapara-AIS, organized by protein 4.1B. BMC Biol. *9*. https://doi.org/10.1186/1741-7007-9-66.

41. Duflocq, A., Le Bras, B., Bullier, E., Couraud, F., and Davenne, M. (2008). Nav1.1 is predominantly expressed in nodes of Ranvier and axon initial segments. Mol. Cell. Neurosci. *39*, 180–192.

42. Van Wart, A., Trimmer, J.S., and Matthews, G. (2007). Polarized distribution of ion channels within microdomains of the axon initial segment. J. Comp. Neurol. *500*, 339–352. https://doi.org/10.1002/cne.21173.

43. Hu, W., Tian, C., Li, T., Yang, M., Hou, H., and Shu, Y. (2009). Distinct contributions of Na(v)1.6 and Na(v)1.2 in action potential initiation and backpropagation. Nat. Neurosci. *12*, 996–1002. https://doi.org/10.1038/nn.2359.

44. Astman, N., Gutnick, M.J., and Fleidervish, I.A. (2006). Persistent Sodium Current in Layer 5 Neocortical Neurons Is Primarily Generated in the Proximal Axon. J. Neurosci. *26*, 3465–3473.

45. Harris, J.B., Boakes, R.J., and Court, J.A. (1992). Physiological and biochemical studies on the cerebellar cortex of the murine mutants "jolting" and "motor end-plate disease. J. Neurol. Sci. *110*, 186–194. https://doi.org/10.1016/0022-510x(92)90027-i.

46. Khaliq, Z.M., Gouwens, N.W., and Raman, I.M. (2003). The contribution of resurgent sodium current to high-frequency firing in Purkinje neurons: an experimental and modeling study. J. Neurosci. *23*, 4899–4912.

47. Raman, I.M., Sprunger, L.K., Meisler, M.H., and Bean, B.P. (1997). Altered Subthreshold Sodium Currents and Disrupted Firing Patterns in Purkinje Neurons of Scn8a Mutant Mice. Neuron *19*, 881–891.

48. Levin, S.I., Khaliq, Z.M., Aman, T.K., Grieco, T.M., Kearney, J.A., Raman, I.M., and Meisler, M.H. (2006). Impaired motor function in mice with cell-specific knockout of sodium channel Scn8a (NaV1.6) in cerebellar purkinje neurons and granule cells. J. Neurophysiol. *96*, 785–793. https://doi.org/10.1152/jn.01193.2005.

49. Mercer, J.N., Chan, C.S., Tkatch, T., Held, J., and Surmeier, D.J. (2007). Nav1.6 sodium channels are critical to pacemaking and fast spiking in globus pallidus neurons. J. Neurosci. *27*, 13552–13566. https://doi.org/10.1523/JNEUROSCI.3430-07.2007.

50. Smith, M.R., Smith, R.D., Plummer, N.W., Meisler, M.H., and Goldin, A.L. (1998). Functional Analysis of the Mouse Scn8a Sodium Channel. J. Neurosci. *18*, 6093–6102.

51. Rush, A.M., Dib-Hajj, S.D., and Waxman, S.G. (2005). Electrophysiological properties of two axonal sodium channels, Nav1.2 and Nav1.6, expressed in mouse spinal sensory neurones. J. Physiol. *564*, 803–815. https://doi.org/10.1113/jphysiol.2005.083089.

52. Burbidge, S.A., Dale, T.J., Powell, A.J., Whitaker, W.R.J., Xie, X.M., Romanos, M.A., and Clare, J.J. (2002). Molecular cloning, distribution and functional analysis of the NAV1.6. Voltage-gated sodium channel from human brain. Brain Res. Mol. Brain Res. *103*, 80–90.

53. Chatelier, A., Zhao, J., Bois, P., and Chahine, M. (2010). Biophysical characterisation of the persistent sodium current of the Nav1.6 neuronal sodium channel: a single-channel analysis. Pflugers Arch. *460*, 77–86. https://doi.org/10.1007/s00424-010-0801-9.

54. Chen, Y., Yu, F.H., Sharp, E.M., Beacham, D., Scheuer, T., and Catterall, W.A. (2008). Functional properties and differential neuromodulation of Na(v)1.6 channels. Mol. Cell. Neurosci. *38*, 607–615. https://doi.org/10.1016/j.mcn.2008.05.009.

55. Royeck, M., Horstmann, M.T., Remy, S., Reitze, M., Yaari, Y., and Beck, H. (2008). Role of axonal NaV1.6 sodium channels in action potential initiation of CA1 pyramidal neurons. J. Neurophysiol. *100*, 2361–2380. https://doi.org/10.1152/jn.90332.2008.

56. Katz, E., Stoler, O., Scheller, A., Khrapunsky, Y., Goebbels, S., Kirchhoff, F., Gutnick, M.J., Wolf, F., and Fleidervish, I.A. (2018). Role of sodium channel subtype in action potential generation by neocortical pyramidal neurons. Proc. Natl. Acad. Sci. USA *115*, E7184–E7192. https://doi.org/10.1073/pnas.1720493115.

57. Enomoto, A., Han, J.M., Hsiao, C.F., and Chandler, S.H. (2007). Sodium currents in mesencephalic trigeminal neurons from Nav1.6 null mice. J. Neurophysiol. *98*, 710–719.

58. Maurice, N., Tkatch, T., Meisler, M., Sprunger, L.K., and Surmeier, D.J. (2001). D1/D5 dopamine receptor activation differentially modulates rapidly inactivating and persistent sodium currents in prefrontal cortex pyramidal neurons. J. Neurosci. *21*, 2268–2277. https://doi.org/10.1523/JNEUROSCI.21-07-02268.2001.

59. Do, M.T.H., and Bean, B.P. (2004). Sodium currents in subthalamic nucleus neurons from Nav1.6-null mice. J. Neurophysiol. *92*, 726–733. https://doi.org/10.1152/jn.00186.2004.

60. Osorio, N., Cathala, L., Meisler, M.H., Crest, M., Magistretti, J., and Delmas, P. (2010). Persistent Nav1.6 current at axon initial segments tunes

spike timing of cerebellar granule cells. J. Physiol. *588*, 651–670. https://doi.org/10.1113/jphysiol.2010.183798.

61. Sharples, S.A., and Miles, G.B. (2021). Maturation of persistent and hyperpolarization-activated inward currents shapes the differential activation of motoneuron subtypes during postnatal development. Elife *10*, e71385. https://doi.org/10.7554/eLife.71385.
62. Kuo, J.J., Lee, R.H., Zhang, L., and Heckman, C.J. (2006). Essential role of the persistent sodium current in spike initiation during slowly rising inputs in mouse spinal neurones. J. Physiol. *574*, 819–834.
63. Swensen, A.M., and Bean, B.P. (2005). Robustness of burst firing in dissociated purkinje neurons with acute or long-term reductions in sodium conductance. J. Neurosci. *25*, 3509–3520. https://doi.org/10.1523/JNEUROSCI.3929-04.2005.
64. Van Wart, A., and Matthews, G. (2006). Impaired firing and cell-specific compensation in neurons lacking nav1.6 sodium channels. J. Neurosci. *26*, 7172–7180. https://doi.org/10.1523/JNEUROSCI.1101-06.2006.
65. Vega, A.V., Henry, D.L., and Matthews, G. (2008). Reduced expression of Na(v)1.6 sodium channels and compensation by Na(v)1.2 channels in mice heterozygous for a null mutation in Scn8a. Neurosci. Lett. *442*, 69–73. https://doi.org/10.1016/j.neulet.2008.06.065.
66. Zhou, W., and Goldin, A.L. (2004). Use-dependent potentiation of the Nav1.6 sodium channel. Biophys. J. *87*, 3862–3872. https://doi.org/10.1529/biophysj.104.045963.
67. Spampanato, J., Escayg, A., Meisler, M.H., and Goldin, A.L. (2001). Functional effects of two voltage-gated sodium channel mutations that cause generalized epilepsy with febrile seizures plus type 2. J. Neurosci. *21*, 7481–7490. https://doi.org/10.1523/JNEUROSCI.21-19-07481.2001.
68. Pambo-Pambo, A., Durand, J., and Gueritaud, J.P. (2009). Early excitability changes in lumbar motoneurons of transgenic SOD1G85R and SOD1G(93A-Low) mice. J. Neurophysiol. *102*, 3627–3642.
69. Miles, G.B., Dai, Y., and Brownstone, R.M. (2005). Mechanisms underlying the early phase of spike frequency adaptation in mouse spinal motoneurones. J. Physiol. *566*, 519–532.
70. Burgess, D.L., Kohrman, D.C., Galt, J., Plummer, N.W., Jones, J.M., Spear, B., and Meisler, M.H. (1995). Mutation of a new sodium channel gene, Scn8a, in the mouse mutant 'motor endplate disease. Nat. Genet. *10*, 461–465. https://doi.org/10.1038/ng0895-461.
71. Tzoumaka, E., Tischler, A.C., Sangameswaran, L., Eglen, R.M., Hunter, J.C., and Novakovic, S.D. (2000). Differential distribution of the tetrodotoxin-sensitive rPN4/NaCh6/Scn8a sodium channel in the nervous system. J. Neurosci. Res. *60*, 37–44.
72. Meisler, M.H., Plummer, N.W., Burgess, D.L., Buchner, D.A., and Sprunger, L.K. (2004). Allelic mutations of the sodium channel SCN8A reveal multiple cellular and physiological functions. Genetica *122*, 37–45. https://doi.org/10.1007/s10709-004-1441-9.
73. Lorincz, A., and Nusser, Z. (2008). Cell-type-dependent molecular composition of the axon initial segment. J. Neurosci. *28*, 14329–14340. https://doi.org/10.1523/JNEUROSCI.4833-08.2008.
74. Duchen, L.W. (1970). Hereditary motor end-plate disease in the mouse: light and electron microscopic studies. J. Neurol. Neurosurg. Psychiatry *33*, 238–250. https://doi.org/10.1136/jnnp.33.2.238.

STAR★METHODS

KEY RESOURCES TABLE

REAGENT or RESOURCE	SOURCE	IDENTIFIER
Antibodies		
polyclonal antibody anti-*Nav1.1*	Merck-Millipore	CAT#AB5204; RRID: AB_91751
polyclonal antibody anti-*Nav1.6*	Alomone	CAT#ASC009; RRID : AB_2040202
polyclonal antibody anti-Ankyrin G	Clinisciences	CAT#SC-28561; RRID : AB_633909
monoclonal anti-pan Na_v	Sigma-Aldrich	CAT#S8809; RRID : AB_477552
monoclonal anti-Ankyrin G	Merck-Millipore	CAT #MABN466; RRID : AB_2749806
Alexa Fluor® 488- anti-mouse IgG	Lifetechnologies	CAT#A-11017; RRID : AB_2534084
Alexa Fluor® 546-*anti*-rabbit IgG	Lifetechnologies	CAT#A-11071; RRID : AB_2534115
polyclonal horseradish peroxidase-conjugated anti-mouse IgG	ThermoFisher	CAT#31430; RRID : AB_228307
Bacterial and virus strains		
Ultra-purified custom shRNA AAV2-retro virus (typical titer: >2x10^{13} GC/ml, minimum titer: >10^{13} GC/mL)	Vector Builder	N/A
Chemicals, peptides, and recombinant proteins		
NaCl	Sigma-Aldrich	CAT# 71376
KCl	Sigma-Aldrich	CAT# P3911
NaH_2PO_4	Sigma-Aldrich	CAT# S0751
$MgSO_4$	Sigma-Aldrich	CAT# 1880
$CdCl_2$	Sigma-Aldrich	CAT# 208299
$CaCl_2$	Sigma-Aldrich	CAT# 21115
$NaHCO_3$	Sigma-Aldrich	CAT# S6014
D-glucose	Sigma-Aldrich	CAT# G8270
K^+-gluconate	Sigma-Aldrich	CAT# P1847
$MgCl_2$	Sigma-Aldrich	CAT# M8266
HEPES	Sigma-Aldrich	CAT# H3375
EGTA	Sigma-Aldrich	CAT# E3889
ATP	Sigma-Aldrich	CAT# A9062
GTP	Sigma-Aldrich	CAT# G9002
Sucrose	Sigma-Aldrich	CAT# S9378
Tetraethylammonium chloride	Sigma-Aldrich	CAT# T2265
N-methyl-DL-aspartic acid	Sigma-Aldrich	CAT# M2137
5-hydroxytryptamine creatinine sulfate	Sigma-Aldrich	CAT# S2805
kynurenic acid	Sigma-Aldrich	CAT# K3375
ICA121431	Tocris Bioscience	CAT#5066/10
4,9-Anhydrotetrodotoxin	Tocris Bioscience	CAT# 6159
Paraformaldehyde	Ficher Scientific	CAT# 50-980-495
Phosphate Buffered Saline	Argene Biomérieux	CAT# 33-011
Tissue-Tek OCT compound	VWR	CAT# 25608-930
Triton X-100	Sigma-Aldrich	CAT# T9284
Bovine Serum Albumin	Sigma-Aldrich	CAT# A7906
iodoacetamide	Sigma-Aldrich	CAT# I1149
Trizma hydrochloride	Sigma-Aldrich	CAT# T3253
Trizma base	Sigma-Aldrich	CAT# T1503
Experimental models: Organisms/strains		
C57BL/6 mice	Charles River Laboratories	RRID:IMSR_CRL:643
Nav1.$1^{-/-}$ mice, 129S-Scn1atm1Kea/Mmjax	The Jackson Laboratory	RRID:MMRRC_037107-JAX

(*Continued on next page*)

Continued

REAGENT or RESOURCE	SOURCE	IDENTIFIER
Nav1.6$^{-/-}$ mice, C3Fe.Cg-*Scn8a*^{med}/J	The Jackson Laboratory	RRID:IMSR_JAX:003798
Oligonucleotids		
Nav1.6 targeting sequence TTGTCCTGAACACACTATTTA	Vector Builder	ID: VB201204-1040dts
Scrambled sequence CCTAAGGTTAAGTCGCCCTCG	Vector Builder	ID: VB190708-1058bsm
Software and algorithms		
Clampex 10	Molecular Devices	v10.3
Clampfit 10	Molecular Devices	v10.3
Graphpad Prism	Prism	RRID: SCR_002798
Zen2.6 (Blue Edition)	Zeiss	V2.6
Catwalk xt10.6	https://www.noldus.com/catwalk-xt	V10.6
Other		
Vibrating microtome	Leica	VT1000S
Temperature controller	Warner Instruments	CL-100
Nikon Eclipse microscope	Nikon	E600FN
Confocal microscope	Zeiss	LSM700
Infrared-sensitive CCD camera	Roper Scientific GmbH	N/A
Digidata 1550b interface	Molecular Devices	N/A
Multiclamp 700B amplifier	Molecular Devices	N/A
Borosilicate glass capillaries	World Precision Instruments	CAT# TW150-4
Sutter P-97 puller	Sutter Instruments	P-97
Knittel Glass coverslips	Dutscher	CAT# 900529
Polysine slides	Thermoscientific	CAT# P4981

RESOURCE AVAILABILITY

Lead contact

Further information and requests for resources and reagents should be directed to and will be fulfilled by the Lead Contact, Frédéric Brocard (frederic.brocard@univ-amu.fr).

Materials availability

This study did not generate new unique reagents.

Data and code availability

- All data reported in this paper will be shared by the lead contact upon request.
- This paper does not report original code.
- Any additional information required to reanalyze the data reported in this paper is available from the lead contact upon request.

EXPERIMENTAL MODEL AND SUBJECT DETAILS

Mice

Mice (C57/Bl6 background) of either sex (P2-P3 for fictive locomotion experiments, P8-P14 for patch-clamp recordings, P14-P28 for behavioral experiments) were housed under a 12h light/dark cycle with *ad libitum* access to water and food. Room temperature was kept between 21°C and 24°C and between 40 and 60% relative humidity. Mice heterozygous for the Scn1a (Nav1.1$^{+/-}$) and Scn8a^{med} (*Nav1.6*$^{+/-}$) were purchased from the Jackson laboratory (Bar Harbor, ME). Only homozygous animals were studied. All animal care and use were in compliance with the French regulations (Décret 2010-118) and approved by the ethics committee (Comité d'Ethique en experimentation animale, CEEA-071 Nb A1301404, authorization Nb 2018110819197361).

METHOD DETAILS

shRNA construct

Specific shRNA sequence designed to knockdown Nav1.6 transcript (TTGTCCTGAACACACTATTTA) was incorporated into a recombinant adeno-associated viral vector serotype 2 retrograde (rAAV2-retro), which features a U6 polymerase promoter to drive shRNA expression and a CMV promoter to drive eGFP expression for identification of transduced neurons (Vector Builder, Chicago, IL). We also used a non-targeting shRNA sequence (CCTAAGGTTAAGTCGCCCTCG) which has no homology to any known genes in mouse as a control. The standard titers of AAVs were $\geq 1 \times 10^{13}$ GC/mL (genome copies/ml).

Intramuscular vector delivery

The rAAV2-retro has been reported to extensively and high-efficiently transduce spinal motoneurons following a single intramuscular injection in neonatal mice.[39] This technique was therefore chosen by unilaterally injecting the *triceps surae* muscle. Briefly, in pups cryoanesthetized at P2, the tip of the microcapillary preloaded with the AAV particles was lowered into the center of the muscle under optical microscope control. A total volume of 1.5 μL/animal was then slowly injected by hand with the micropipette held in place for an additional 30 s after injection before being slowly retracted.

In vitro preparations

For the slice preparation, the lumbar spinal cord was isolated in ice-cold (+4°C) artificial CSF (aCSF) solution composed of the following (in mM): 252 sucrose, 3 KCl, 1.25 NaH_2PO_4, 4 $MgSO_4$, 0.2 $CaCl_2$, 25 $NaHCO_3$, 20 D-glucose, pH 7.4. The lumbar spinal cord was then introduced into a 1% agar solution, quickly cooled, mounted in a vibrating microtome (Leica, VT1000S) and sliced (325 μm) through the L1-L2 or L3-L5 lumbar segments. Slices were immediately transferred into the holding chamber filled with bubbled (95% O_2 and 5% CO_2) aCSF solution composed of (in mM): 120 NaCl, 3 KCl, 1.25 NaH_2PO_4, 1.3 $MgSO_4$, 1.2 $CaCl_2$, 25 $NaHCO_3$, 20 D-glucose, pH 7.4, 30°C–32°C. After a 30–60 min resting period, individual slices were transferred to a recording chamber continuously perfused with aCSF heated to 32°C–34°C. *For the whole-spinal cord preparation,* the spinal cord was transected at T8-9, isolated and transferred with intact dorsal and ventral roots to the recording chamber. The tissue was continuously bubbled (95% O_2 and 5% CO_2) and perfused with heated (~27°C–28°C) aCSF solution composed of (in mM): 120 NaCl, 4 KCl, 1.25 NaH_2PO_4, 1.3 $MgSO_4$, 1.2 $CaCl_2$, 25 $NaHCO_3$, 20 D-glucose, pH 7.4.

In vitro recordings. For the slice preparation, whole-cell patch-clamp recordings were performed using a Multiclamp 700B amplifier (Molecular Devices) from L_3-L_5 motoneurons with the largest soma (>400μm^2) located in the lateral ventral horn or from L_1-L_2 ventromedial interneurons adjacent to the central canal, a region proposed to contain a large part of the rhythm-generating locomotor network.[35] Patch electrodes (2–4 MΩ) were pulled from borosilicate glass capillaries (1.5 mm OD, 1.12 mm ID; World Precision Instruments) on a Sutter P-97 puller (Sutter Instruments Company) and filled with intracellular solution containing (in mM): 140 K^+-gluconate, 5 NaCl, 2 $MgCl_2$, 10 HEPES, 0.5 EGTA, 2 ATP, 0.4 GTP, pH 7.3 (280–290 mOsm). Pipette and neuronal capacitive currents were canceled and, after breakthrough, the series resistance was compensated and monitored. Recordings were digitized on-line and filtered at 10 kHz through a Digidata 1322A interface using Clampex 10.3 software (Molecular Devices). The main characterization of I_{NaP} was accomplished by slow ramp increase from −70 mV to −10 mV, slow enough (12 mV/s) to prevent transient sodium channel opening. All experiments were designed to gather data within a stable period (i.e., at least 5 min after establishing whole-cell access). For the whole spinal cord preparation, motor outputs were recorded from lumbar ventral roots by means of glass suction electrodes connected to an AC-coupled amplifier. The ventral root recordings were amplified (×1,000), high-pass filtered at 100 Hz, low-pass filtered at 5 kHz, and sampled at 10 kHz. Custom-built amplifiers enabled simultaneous online rectification and integration (100 ms time constant) of raw signals. Locomotor-like activity was induced by a bath application of N-methyl-DL aspartate (NMA, 10 μM) and 5-hydroxytryptamine (5-HT, 10 μM). In some experiments, a Vaseline barrier was built at the L_2/L_3 level to superfuse the highly rhythmogenic region of the locomotor network located in the rostral lumbar cord independently from the lumbar enlargement where most of motoneurons are present.

Assessment of motor behaviors

Walking. The CatWalkXT (Noldus Information Technology, Netherlands) was used to measure walking performance. Each animal walked freely through a corridor on a glass walkway illuminated with beams of light from below. A successful walking trial was defined as having the animal walk at a steady speed (no stopping, rearing, or grooming), and three to five successful trials were collected per animal. Footprints were recorded using a camera positioned below the walkway while a second camera placed parallel to the corridor captured hindlimb movements of the right side. The paw print and kinematic parameters were then analyzed using the CatWalk and the deepLabCut softwares, respectively. *Rotarod test.* Mice were placed on a rotarod (Bioseb) accelerating from 4 to 40 rpm over a span of 5 min. Mice were given 3 trials with a 30-s inter-trial interval.

Immunostaining

Spinal cords from 2-wk-old mice were dissected and immersion-fixed for 1 h in 0.25% paraformaldehyde (PFA), then rinsed in phosphate buffered saline (PBS) and cryoprotected overnight in 20% sucrose at 4°C. Spinal cords were frozen in OCT medium (Tissue Tek) and 30 μm cryosections were collected from the L1-L2 and L4-L5 segments. Slices were rehydrated in PBS at room temperature for 15 min, permeated for 1 h in a blocking solution (BSA 1%, Normal Donkey Serum 3% in PBS) with 0.2% Triton X-100, and for 12 h at 4°C in a humid chamber with the primary polyclonal antibody anti-*Nav1.1* (1:400; #AB5204, Merck-Millipore from rabbit), or anti-*Nav1.6* (1:200; #ASC009, Alomone from rabbit) or anti-Choline Acetyltransferase (1/200; AB144P, Sigma-Aldrich) or anti-Ankyrin G (1:500; #SC-28561, Clinisciences from rabbit), or with the primary monoclonal anti-pan Na_v (1:1000, #S8809,Sigma from mouse) or anti-Ankyrin G (1:500; #MABN466, Merck-Millipore from mouse). Slices were then washed 3 × 5 min in PBS and incubated for 2 h with Alexa Fluor 488-*anti*-mouse or 546-*anti*-rabbit or 546-*anti*-goat IgG secondary antibodies (1:800, 1:400, 1:400, #A-11017, #A-11071, A-11056, Lifetechnologies). After 3 washes of 5 min in PBS, they were mounted with a gelatinous aqueous medium. Sections were scanned using a laser scanning confocal microscope (Zeiss LSM700) in stacks of 0.3–1 μm-thick optical sections at × 63 and/or ×20 magnification respectively and processed with the Zen 12.0 software (Zeiss). Each optical section resulted from two scanning averages. Each figure corresponds to a projection image from a stack of optical sections. We used identical settings, finely tuned to avoid saturation, for the whole series.

Nav channels protein quantification

Membrane protein isolation and Western blots. Tissues were collected from spinal cord lumbar enlargements and frozen after removing the dorsal and ventral roots. For the membrane fraction, corresponding to the plasma membrane-enriched fraction, samples were homogenized in ice-cold lysis buffer (320 mM sucrose, 5 mM Tris-HCL pH 7.5, 10 μM iodoacetamide) supplemented with protease inhibitors (CompleteMini, Roche diagnostic Basel, Switzerland). Unsolubilized material was pelleted by centrifugation at 7,000 g for 5 min. The supernatant was subjected to an additional centrifugation step at 18000g for 70 min at 4°C. Pellets were collected and homogenized in ice-cold lysis buffer (1% Igepal CA-630, Phosphate Buffer Saline 1X, 0.1% SDS, 10 μM iodoacetamide), supplemented with protease inhibitors (CompleteMini, Roche diagnostic). Protein concentrations were determined using a detergent-compatible protein assay (Bio-Rad). Equal protein amounts (30 μg) from samples were size fractionated by 4–15% Mini-PROTEAN TGX stain-free gels (Bio-Rad), transferred to a nitrocellulose membrane and probed with the monoclonal anti-pan Na_v (1:500, #S8809, Sigma from mouse) at 4°C overnight in Tris-buffered saline containing 5% fat-free milk powder. The blot was then incubated for 1 h at 22°C with a polyclonal horseradish peroxidase-conjugated anti-mouse IgG secondary antibody (1:40000; #31430, ThermoFisher). Signal intensities were measured with the image analysis software Quantity-One (BioRad).

Drug list and recording solutions: Normal aCSF was used in most cases for *in vitro* electrophysiological recordings (see above). Ca^{2+}-free solution was made by removing Ca^{2+} chloride from the recording solution and replacing it with an equimolar concentration of magnesium chloride. Neurons were sometimes isolated from glutamatergic excitatory inputs with the kynurenic acid (1.5 mM). To isolate Na^+ currents during voltage-clamp experiments we used a modified aCSF containing (in mM): 100 NaCl, 3 KCl, 1.25 NaH_2PO_4, 1.3 $MgSO_4$, 3.6 $MgCl_2$, 1.2 $CaCl_2$, 25 $NaHCO_3$, 40 D-glucose, 10 TEA-Cl and 0.1 $CdCl_2$. All solutions were oxygenated with 95% O_2/5% CO_2. All salt compounds, tetraethylammonium (TEA; #T2265), N-methyl-DL-aspartic acid (NMA; #M2137), 5-hydroxytryptamine creatinine sulfate (5-HT; #S2805), were obtained from Sigma-Aldrich, 4,9-Anhydrotetrodotoxin (4,9-ahTTX; #6159) and ICA121431 (ICA; #5066/10) from Tocris Bioscience.

QUANTIFICATION AND STATISTICAL ANALYSIS

Data analysis

Electrophysiological data were analyzed offline with Clampfit 10.7 software (Molecular Devices). For whole-cell recordings, several basic criteria were set to ensure optimum quality of intracellular recordings. Only cells exhibiting a stable resting membrane potential, access resistance (no > 20% variation) and an action potential amplitude larger than 40 mV under normal aCSF were considered. Passive membrane properties of cells were measured by determining from the holding potential the largest voltage deflections induced by small current pulses that avoided activation of voltage-sensitive currents. We determined input resistance by the slope of linear fits to voltage responses evoked by small positive and negative current injections. Firing properties were measured from depolarizing current pulses of varying amplitudes. The rheobase was defined as the minimum step current intensity required to induce an action potential. We measured the action potential waveform properties of the first spike elicited by the rheobase sweep. The threshold for action potential was defined as the voltage at the point of deflection for dV/dt to be greater than zero. Peak spike amplitude was measured from the threshold potential, and spike duration was measured at half-amplitude. Action potential slopes (up and down) were measured as maximum slope during the action potential. The instantaneous discharge frequency was determined as the inverse of interspike interval. Firing frequency was calculated as the average action potential frequency over the entire duration of the pulse. All reported membrane potentials were corrected for the liquid junction potential. Bistable properties of motoneurons were investigated with a 2 s suprathreshold depolarizing current pulse elicited from a holding membrane potential at −60 mV. The cell was considered as bistable when (1) the pre-stimulus membrane potential stays below the spiking threshold (downstate), (2) the post-stimulus membrane potential stays depolarized (upstate), at peri-threshold for spike generation and (3) the membrane potential switches to downstate after a brief hyperpolarizing pulse. Bursting properties of interneurons were measured after smoothing to eliminate spikes but preserve the envelope of depolarization. Amplitude and duration of bursts were measured by a threshold function which determines the peak, the onset and the end of bursts. Burst frequency was calculated by dividing the number of bursts by the total duration of the recording. Voltage dependence and kinetics of I_{NaP} were analyzed from normalized voltage-ramp data by fitting them with Boltzmann functions. We defined the voltage-dependent activation threshold of the I_{NaP} as the membrane potential at which the slope of leak-subtracted current first becomes negative. We measured the magnitude of I_{NaP} as the peak of the leak-subtracted inward current during the ascending phase of the voltage command. For extracellular recordings, alternating activity between right/left L5 recordings was taken to be indicative of fictive locomotion. To characterize locomotor burst parameters, raw extracellular recordings from ventral roots were rectified, integrated and resampled at 50 Hz. Peak amplitude and duration of locomotor bursts were measured and the cycle period was calculated by measuring the time between the first two peaks of the auto-correlogram. *Behavioral analyses:* For walking, bottom view recordings were processed by the CatWalk XT software (Noldus Information Technology, Netherlands) to measure a broad number of spatial and temporal gait parameters in several categories. These include (1) the paw print area that refers to the total area of the glass in contact with the paw, measured when the area of contact with the glass is maximal; (2) dynamic parameters related to individual paw prints, such as duration of the step cycle; (3) parameters related to the position of paw prints with respect to each other, for example the hindlimb base of support (the width between the paw pairs); (4) parameters related to time-based relationships between paw pairs. These parameters were calculated for each run and for each paw. To estimate five hindlimb joints positions (toe, ankle, knee, hip and iliac crest) on lateral view videos of freely walking mice, we trained a model using the DeepLabcut toolbox. A total of 320 image frames (16 videos, 20 frames/video) were used to label and train the model. A pre-trained network with 50 layers (ResNet50) was selected and trained for 200 000 iterations. Parameters describing gait timing and joint kinematics were extracted for each gait cycle using a custom-written Python script. Gait cycles were defined as the time interval between two successive paw contacts of one limb. Individual steps were identified within the run by the acceleration of the paws to identify the ‘‘stance’’ and ‘‘swing’’ phases. We measured the total angular excursion for the hip, knee and ankle joints across the cycle for the hindlimbs. In the rotarod test the average latency of the subject to fall was recorded (in seconds). All behavioral tests were carried out with the experimenter blind to the experimental group.

Immunohistochemistry analysis: Quantification of staining intensities were performed with the Zen 12.0 software (Zeiss). Measurements were performed on the axon initial segment (AIS) from interneurons located in the ventromedial part of upper lumbar segments (L_1-L_2) near the central canal and from motoneurons identified as the biggest cells located in the ventral horn (L_4-L_5). The AIS was identified as linear structures labeled by pan Na_v-specific antibodies, and for which the beginning and the end of the structure could be clearly determined. Immunofluorescence intensity profiles were obtained from a line traced along the AIS. For each staining, the background intensity was first subtracted, and immunofluorescence values along each AIS were then normalized to the maximum intensity. The Pearson correlation coefficient was used to quantify the degree of colocalization between fluorophores. The measurements were repeated with similar numbers of motoneurons per animal.

Statistics

No statistical method was used to predetermine sample size. Group measurements were expressed as means ± s.e.m. When two groups (control vs. transgenic mice) were compared, we used the unpaired Mann–Whitney test or the Unpaired *t* test. Fisher test was used to compare the percentages of bistability. When two conditions (control vs. drugs) were compared, we used the Wilcoxon matched pairs test. We also used the one-way or two-way ANOVA tests for multiple comparisons. For all statistical analyses, the data met the assumptions of the test and the variance between the statistically compared groups was similar. The level of significance was set at $p < 0.05$. Statistical analyses were performed using Graphpad Prism 7 software and are indicated in Figure legends.

Cell Reports, Volume *42*

Supplemental information

Persistent Nav1.1 and Nav1.6 currents drive spinal locomotor functions through nonlinear dynamics

Benoît Drouillas, Cécile Brocard, Sébastien Zanella, Rémi Bos, and Frédéric Brocard

SUPPLEMENTARY INFORMATION

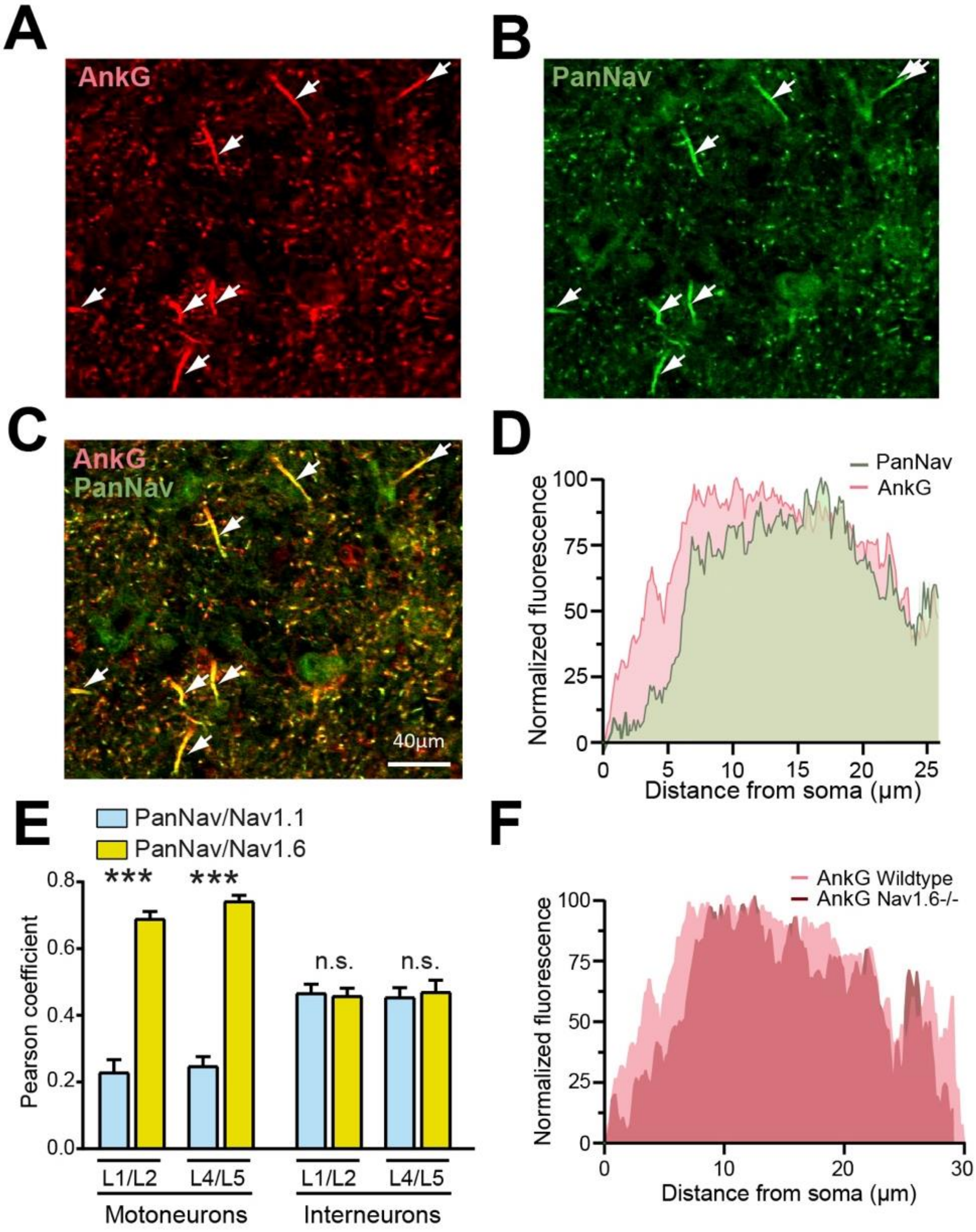

Supplementary Figure. 1 (related to Figure.1): Distribution of Nav channels along the axon initial segments (AISs) of spinal neurons. A-C Confocal images of the ventral horn from wildtype mice (*n* = 2 mice) double-labelled with anti-ankyrin-G (**A**, red) and PanNav (**B**, green) antibodies; Merge image (**C**); Scale bar represent 40 µm. Arrowheads point to axon initial segments (AISs) from presumptive motoneurons. **D** Mean fluorescence intensity profile for the PanNav (green), along the ankyrin-G-labelled AIS (red) of motoneurons (*n* = 7 cells). **E** Pearson's coefficient between PanNav and *Na1.1* (cyan) or between PanNav and *Nav1.6* (yellow) in motoneurons (*n* = 17–43 cells) and interneurons (*n* = 18–39 cells) from L1/L2 or L4/L5 lumbar segments. **F** Mean fluorescence intensity profile for the ankyrin-G along the AIS of motoneurons from wildtype (pink, *n* = 7 cells from 2 mice) and *Nav1.6*$^{-/-}$ (red, *n* = 5 cells from 2 mice) mice. Numbers in brackets in **E** indicate the numbers of cells. Error bars: Mean ± SEM.

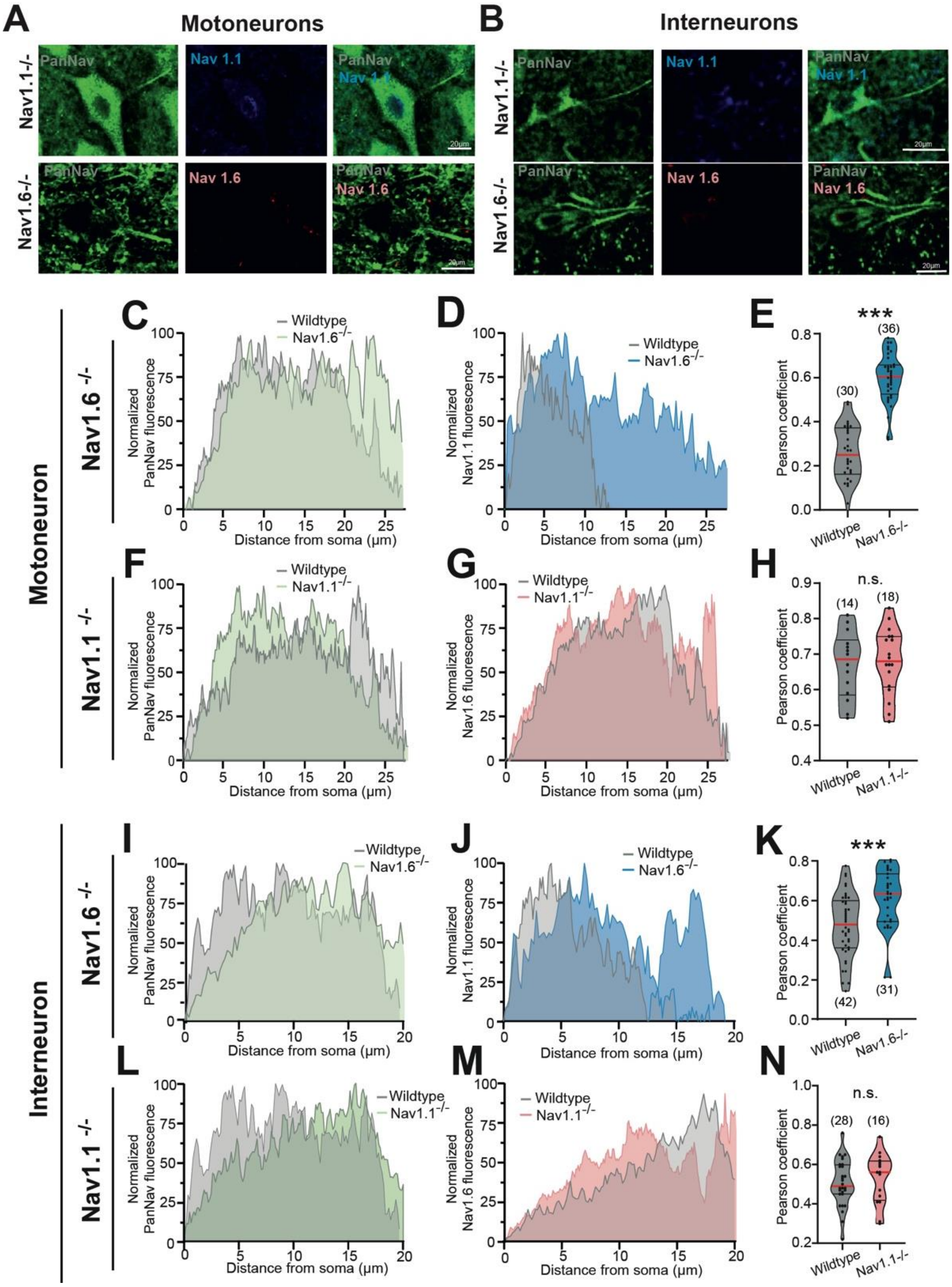

Supplementary Figure. 2 (related to Figure.1): Distribution of Nav channels along the axon initial segments (AISs) of spinal neurons in mutant mice. A,B Representative optical sections showing the immunostaining of all Nav α-subunits (left, green panels), *Nav1.1* subunits (middle-top, blue panels) or *Nav1.6* subunits (middle-low, red panels) along the AISs (arrowheads) of lumbar L4/L5 motoneurons (**A**) or L1/L2 ventromedial interneurons (**B**) in Nav1.1$^{-/-}$ (top panels, $n = 2$) or Nav1.6$^{-/-}$ (low panels, $n = 2$) mutant mice. The right panels are merged images. **C-N** Mean fluorescence intensity profile for the PanNav (**C,F,I,L**), *Nav1.1* (**D,J**) and *Nav1.6* (**G,M**) immunostaining along the PanNav-labelled AIS of both motoneurons (**C,D,F,G,** n = 5–7 cells) and interneurons (**I,J,L,M,** n = 5–10 cells) from *Nav1.1*$^{-/-}$ (**F,G,L,M**) and *Nav1.6*$^{-/-}$ (**C,D,I,J**) mice. For each antibody, the immunofluorescence was normalized to its maximum intensity. **E,H,K,N** Violin plots of the Pearson's coefficient between PanNav and Na1.1 (**E,K**) or between PanNav and *Nav1.6* (**H,N**) in motoneurons (**E,H**) and interneurons (**K,N**) from *Nav1.1*$^{-/-}$ (**H,N**) and *Nav1.6*$^{-/-}$ (**E,K**) mice. Numbers in brackets in **E,H,K,N** indicate the numbers of cells. Each dot represents an individual neuron. n.s., no significance; ***$P <$ 0.001 (Unpaired t-test for **E,H,K,N**).

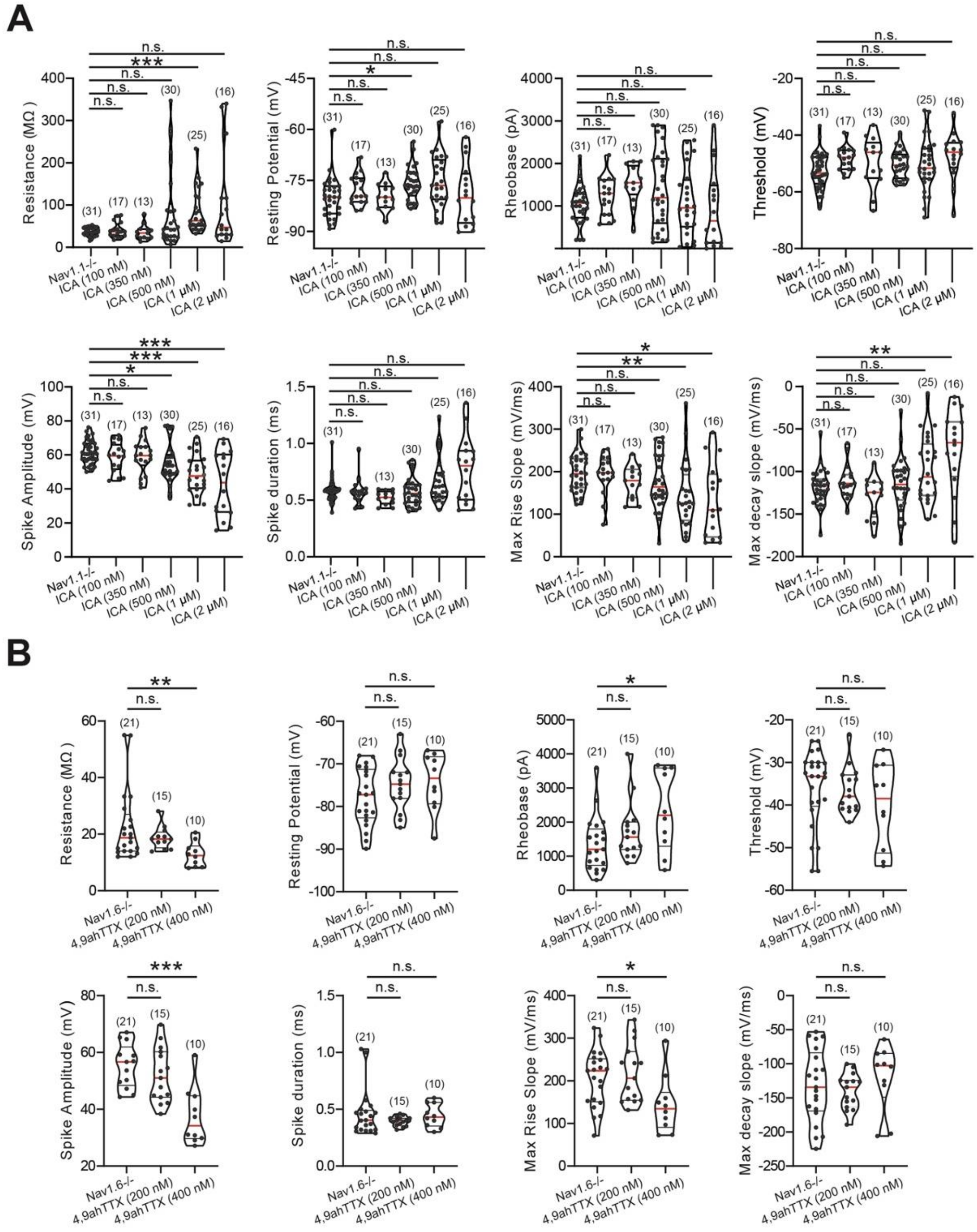

Supplementary Figure. 3 (related to Figure. 2): Determination of the optimal concentration of ICA-121431 and 4,9-anhydrotetrodotoxin to inhibit *Nav1.1* and *Nav1.6* channels, respectively. A,B Violin plots quantifying the effects of ICA-121431 (**A,** ICA, *n* = 9 mice) and 4,9-anhydrotetrodotoxin (**B,** 4,9 ahTTX, *n* = 5 mice) across different concentrations on passive and active membrane properties of *Nav1.1*$^{-/-}$ (*n* = 13–31 cells) and *Nav1.6*$^{-/-}$ (*n* = 10–21 cells) motoneurons, respectively. Numbers in brackets indicate the numbers of motoneurons. Each dot represents an individual motoneuron. n.s., no significance; *$P < 0.05$; **$P < 0.01$; ***$P < 0.001$ (one-way ANOVA with multiple comparisons for **A** and **B**).

Supplementary figure 4

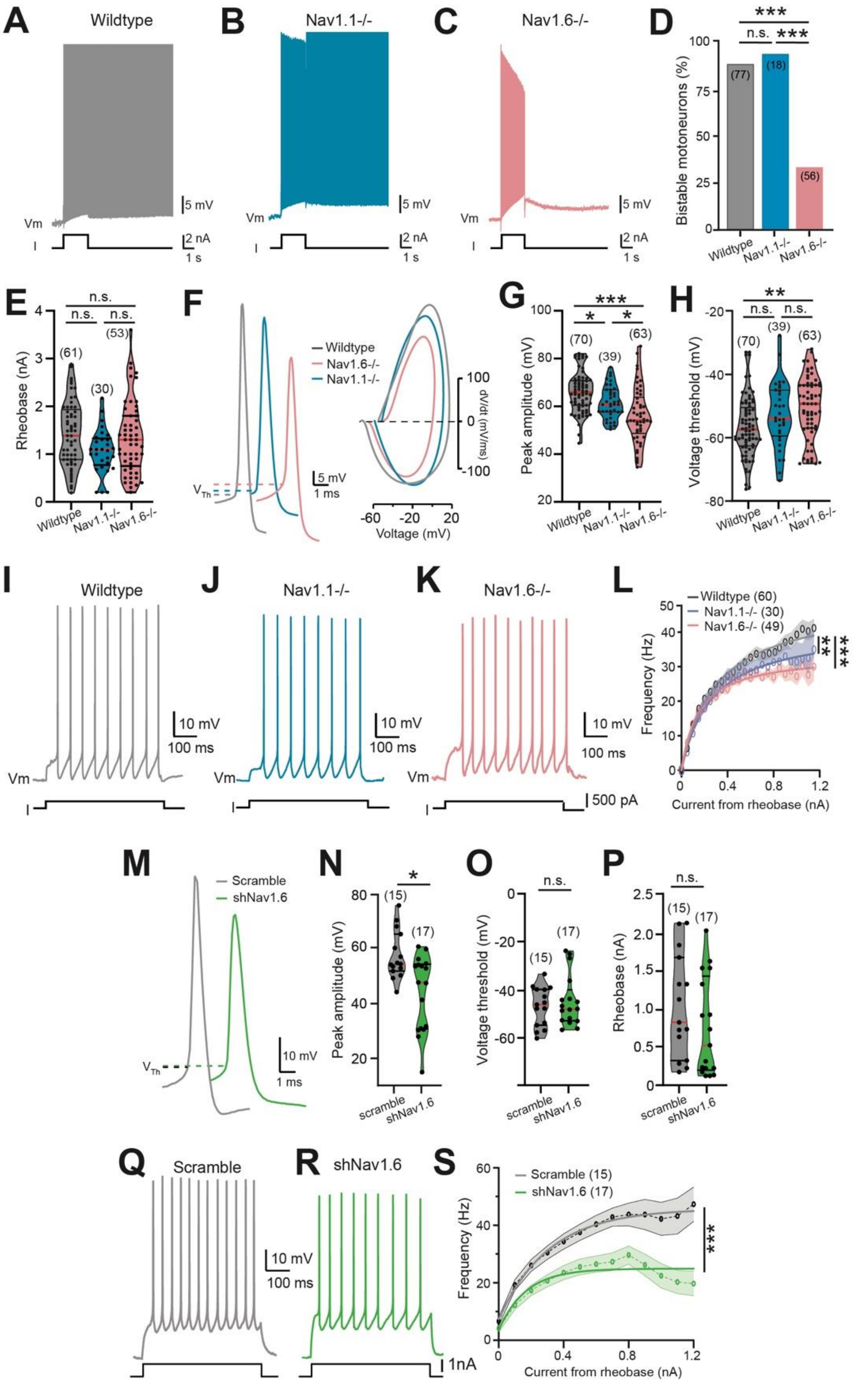

Supplementary Figure. 4 (related to Figure. 2 and 6): Altered bistability of lumbar motoneurons lacking *Nav1.6*. A-C,F,I-K,M,Q,R Voltage traces from motoneurons in response to suprathreshold (**A-C**), near-threshold (**F,M**) or incrementing (**I-K,Q,R**) depolarizing pulses recorded from wildtype (**A**,**F,I,** grey, *n* = 6 mice), *Nav1.1*$^{-/-}$ (**B,F,J**, blue, *n* = 5 mice) and *Nav1.6*$^{-/-}$ (**C,F,K**, pink, *n* = 7 mice) mice or from mice transduced either with the scramble shRNA (**M,Q,R,** grey, *n* = 3 mice) or with the *Nav1.6*-shRNA (**M,Q,R,** green, *n* = 4 mice). **D** Quantification of the proportion of bistable motoneurons (*n* = 18–77 cells). **E,G,H** Violin plots of the rheobase (**E,P**), peak amplitude (**G,N**) and threshold (**H,O**) of the action potential (*n* = 15–70 cells). **F,M** Representative individual action potentials recorded in motoneurons from wildtype/scramble (grey), *Nav1.1*$^{-/-}$ (blue), *Nav1.6*$^{-/-}$ (pink) or *Nav1.6*-shRNA-transduced (green) mice with their phase plots (right) generated from the first derivative (dV/dt; y-axis) versus membrane potential (mV; x-axis). Dashed lines indicate the spiking threshold (V_{Th}). **L,S** Firing frequency as a function of the amplitude of the current pulse (*n* = 15–60). Continuous lines represent best fit functions for experimental data with 95% confidence interval. Numbers in brackets in **D,E,G,H,L,N-P,S** indicate the numbers of motoneurons. Each dot represents an individual cell. n.s., no significance; **P* < 0.05; ***P* < 0.01; ****P* < 0.001 (two-tailed Fisher test for **D**; one-way ANOVA with multiple comparisons for **E,G,H**; two-tailed Mann-Whitney test for **N-P**; comparison of the fits for **L,S**).

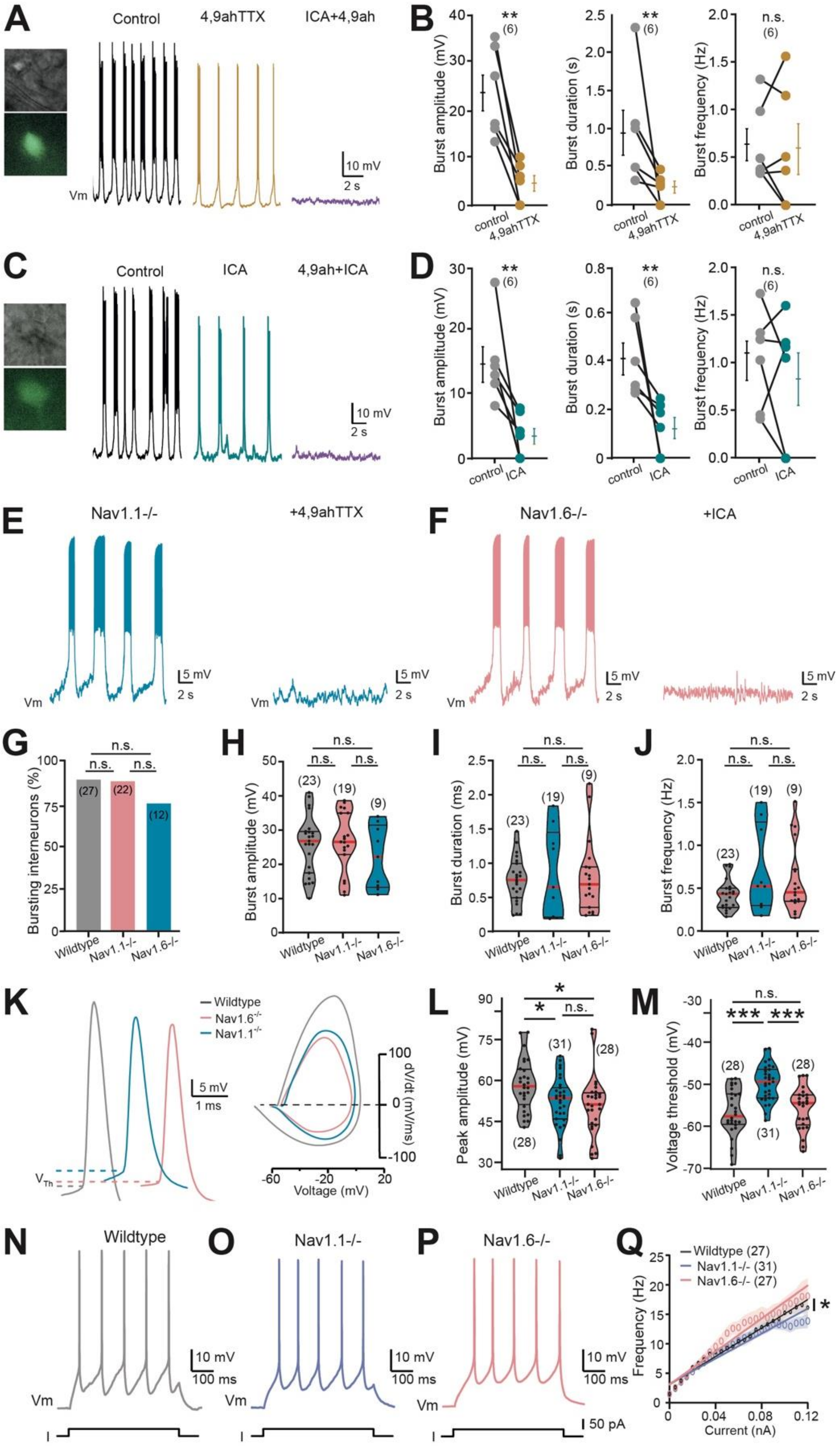

Supplementary Figure. 5 (related to Figure. 3): I_{NaP}-dependent bursting properties in Hb9:GFP and mutant mice. A,C [Ca^{2+}]$_o$-free-saline-induced bursting activity recorded from locomotor related Hb9:GFP interneurons (L_1-L_2) before and after adding 4,9-anhydrotetrodotoxin (**A**, 4,9 ahTTX, 200 nM, *n* = 6 cells from 2 mice) or ICA-121431 (**C**, ICA, 350 nM, *n* = 6 cells from 2 mice) or when the two drugs were co-applied. **B,D** Quantification of burst parameters. **E,F** $[Ca^{2+}]_o$-free-saline-induced bursting activity recorded from ventromedial interneurons of the locomotor CPG region (L_1-L_2) in *Nav1.1*$^{-/-}$ mice (**E**) before (left) and during (right) the bath application of 4,9-anhydrotetrodotoxin (4,9 ahTTX, 200 nM, *n* = 2 mice) or in *Nav1.6*$^{-/-}$ mice (**F**) before (left) and during (right) the bath application of ICA-121431 (ICA, 350 nM, *n* = 2 mice). **G** Quantification of the proportion of bursting cells (*n* = 12–27). **H-J** Quantification of burst parameters (*n* = 9–23 cells). **K** Representative individual action potentials (left) recorded in interneurons from wildtype (grey), *Nav1.1*$^{-/-}$ (blue) or *Nav1.6*$^{-/-}$ (pink) mice with their phase plots (right) generated from the first derivative (dV/dt; y-axis) versus membrane potential (mV; x-axis). Dashed lines indicate the spiking threshold (V_{Th}). **L,M** Violin plots of the peak amplitude (**L**) and threshold (**M**) of the action potential (*n* = 28–31 cells). **N-P** Voltage traces from interneurons in response to incrementing depolarizing pulses recorded from wildtype (**N,** *n* = 7 mice), *Nav1.1*$^{-/-}$ (**O,** *n* = 3 mice) or *Nav1.6*$^{-/-}$ (**P,** *n* = 7 mice) mice. **Q** Firing frequency as a function of the amplitude of the current pulse (*n* = 27–31 cells). Continuous lines represent best fit functions for experimental data with 95% confidence interval. Numbers in brackets in **H-J,L,M,Q** indicate the number of interneurons. Each dot represents an individual cell. n.s., no significance; $^{*}P < 0.05$; $^{***}P < 0.001$ (two-tailed Fisher test for **G**; one-way ANOVA with multiple comparisons for **H-J,L,M**; comparison of the fits for **Q**). Error bars: Mean ± SEM.

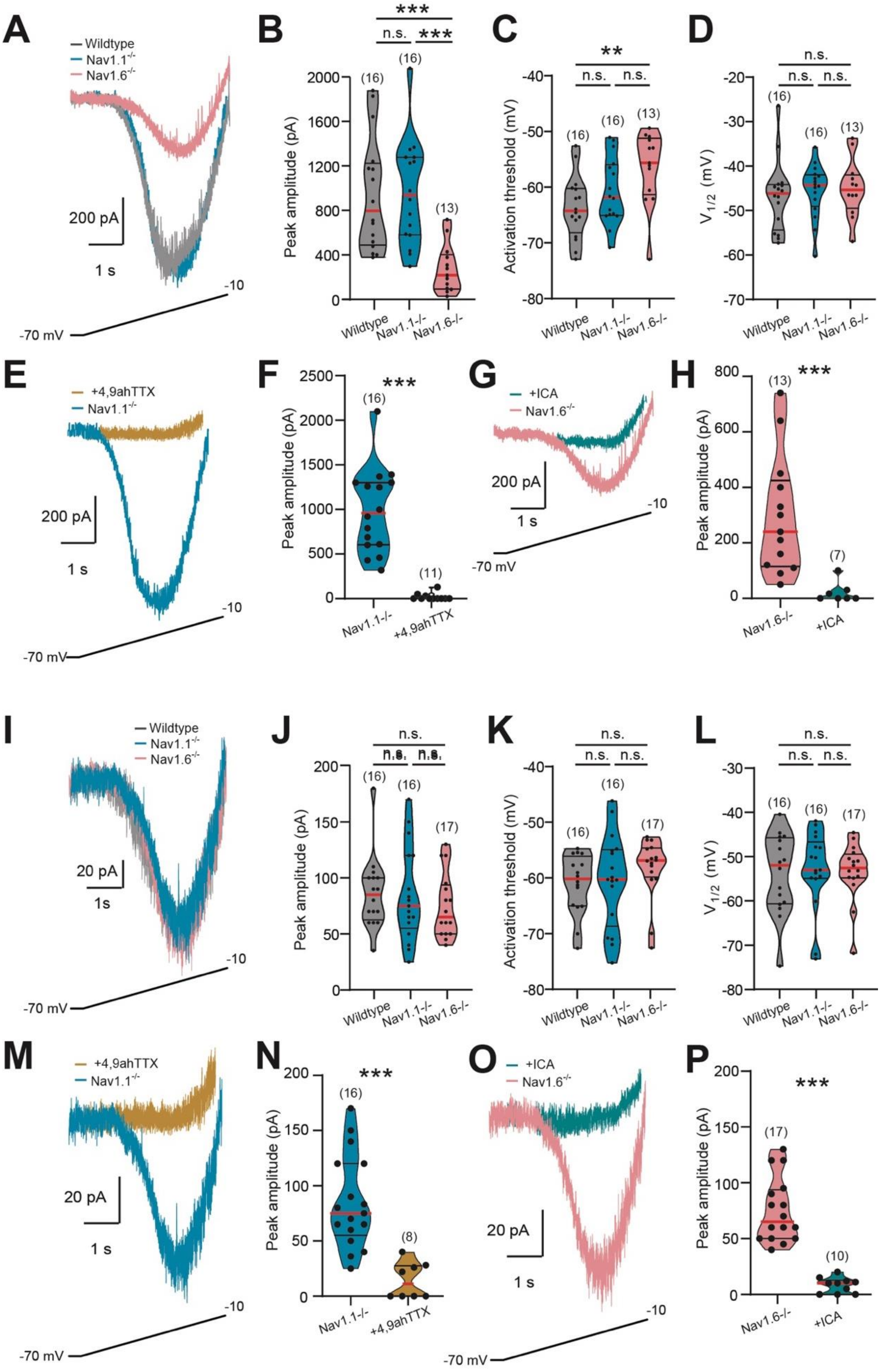

Supplementary Figure. 6 (related to Figure. 4): Motoneurons lacking the *Nav1.6* subunits display reduced I_{NaP}. A,I Leak-subtracted I_{NaP} recorded in motoneurons (**A**, *n* = 13–16 cells) and interneurons of the CPG region (**I**, *n* = 16–17 cells) from wildtype (grey, *n* = 3 mice), *Nav1.1*$^{-/-}$ (blue, *n* = 3 mice) and *Nav1.6*$^{-/-}$ (pink, *n* = 2 mice) mice in response to a slow ramping depolarization. **E,M** Leak-subtracted I_{NaP} recorded in motoneurons (**E**, *n* = 11–16 cells) and interneurons of the CPG region (**M**, *n* = 8–16 cells) from *Nav1.1*$^{-/-}$ mice (*n* = 3) with or without the bath application of 4,9-anhydrotetrodotoxin (4,9 ahTTX, 200 nM). **G,O** Leak-subtracted I_{NaP} recorded in motoneurons (**G**, *n* = 7–13 cells) and interneurons of the CPG region (**O**, *n* = 10–17 cells) from *Nav1.6*$^{-/-}$ mice with and without the bath application of ICA-121431 (ICA, 350 nM). **B-D,F,H,J-L,N,P** Quantification of biophysical properties of I_{NaP}. Numbers in brackets indicate the number of neurons. Each dot represents an individual neuron. n.s., no significance; $^{**}P < 0.01$; $^{***}P < 0.001$ (two-tailed Mann-Whitney test for **F,H,N,P**; one-way ANOVA with multiple comparisons for **B-D,J-L**).

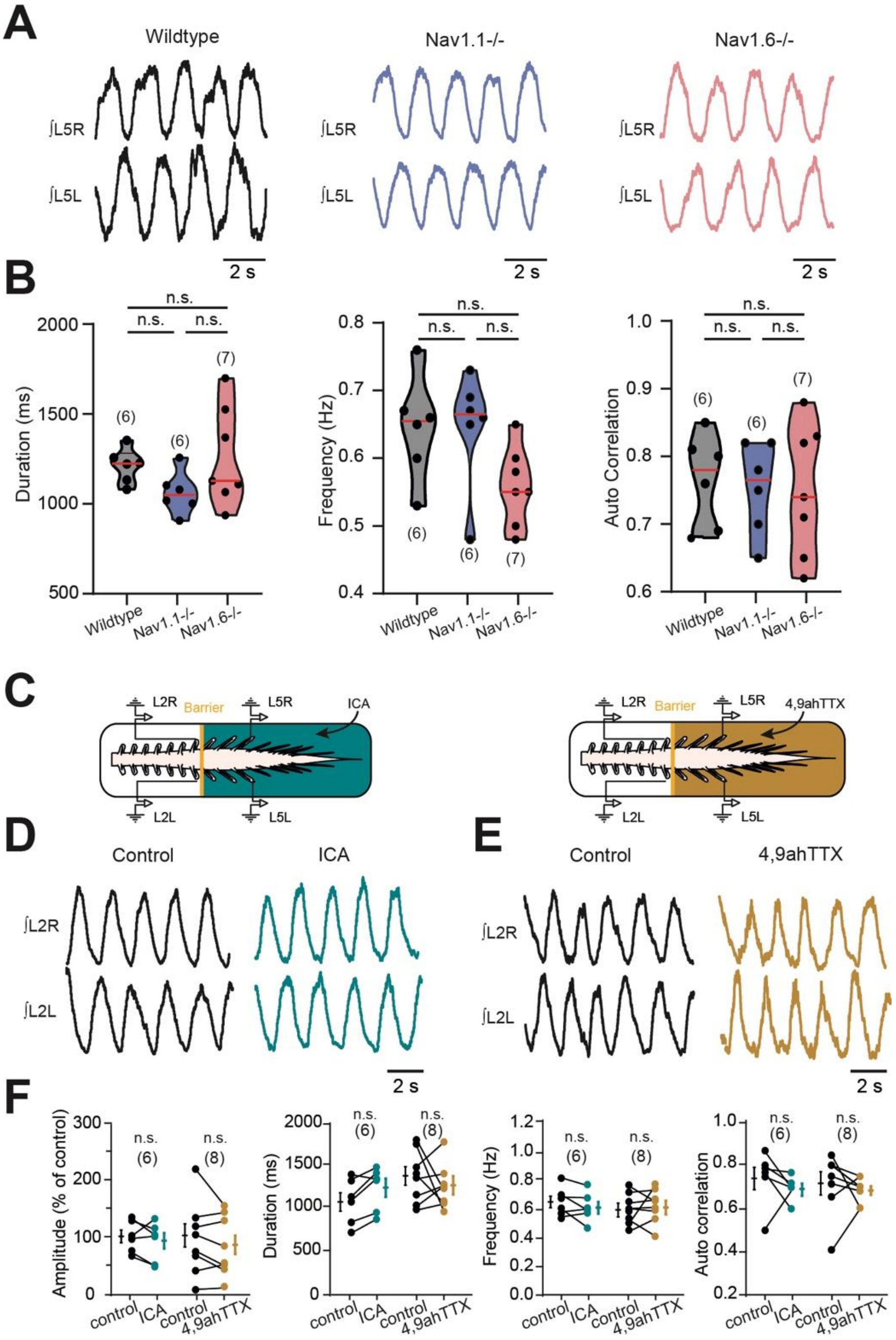

Supplementary Figure. 7 (related to Figure. 5): Spinal cords isolated from *Nav1.1*$^{-/-}$ and *Nav1.6*$^{-/-}$ mutant mice display normal fiction locomotion. A L5 Ventral-root recordings of NMA/5-HT-induced fictive locomotor activity recorded in spinal cords isolated from wildtype (left, black, n = 6), *Nav1.1*$^{-/-}$ (middle, blue, n = 6) or *Nav1.6*$^{-/-}$ (right, pink, n = 7) mice. **B,F** Quantification of locomotor burst parameters. **C** Schematic representation of the whole-mount spinal cord with the recording glass electrodes from homosegmental L$_2$-L$_5$ (R/L). The yellow solid line represents the Vaseline barrier. Built at L$_2$/L$_3$ level the Vaseline barrier allows the selective application of drugs over the rostral (above L_3 segment) or the caudal lumbar segments (below L_3 segment). **D,E** L2 Ventral-root recordings of NMA/5-HT-induced fictive locomotor activity recorded in spinal cords isolated from wildtype mice before and after adding ICA-121431 (**D**, ICA, 350 nM, $n = 6$) or 4,9-anhydrotetrodotoxin (**E**, 4,9 ahTTX, 200 nM, $n = 8$) to caudal lumbar segments. Numbers in brackets in **B,F** indicate the number of spinal cords. Each dot represents an individual spinal cord. n.s., no significance (one-way ANOVA with multiple comparisons for **B**; two-tailed Wilcoxon paired test for **F**). Error bars: Mean ± SEM.